Progress in Oceanography 199 (2021) 102707

Contents lists available at ScienceDirect

Progress in Oceanography

journal homepage: www.elsevier.com/locate/pocean

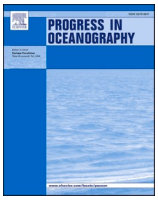

Ice, wind, and water: Synoptic-scale controls of circulation in the Chukchi Sea

Bridget Ovall [a,b,*], Robert S. Pickart [a], Peigen Lin [a], Phyllis Stabeno [c], Thomas Weingartner [d], Motoyo Itoh [e], Takashi Kikuchi [e], Elizabeth Dobbins [d], Shaun Bell [c,f]

[a] Woods Hole Oceanographic Institution, Woods Hole, MA 02543, USA
[b] Department of Marine and Coastal Sciences, Rutgers University, New Brunswick, NJ 08901, USA[1]
[c] Pacific Marine Environmental Laboratory, National Oceanic and Atmospheric Administration, Seattle, WA, USA
[d] College of Fisheries and Ocean Sciences, University of Alaska, Fairbanks, AK 99775, USA
[e] Institute of Arctic Climate and Environment Research, Japan Agency of Marine-Earth Science and Technology, Yokosuka, Japan
[f] Joint Institute for the Study of the Atmosphere and Oceans, University of Washington, Box 354235, Seattle, WA 98195-4235, USA

ARTICLE INFO

Keywords:
Arctic Ocean
Chukchi Sea
Barrow Canyon and Bering Strait
Coastal upwelling
Wind-driven circulation
Sea ice
Polynyas
Pacific Water
Atlantic Water

ABSTRACT

A composite dataset of 27 moorings across the Chukchi Sea and Bering Strait in 2013–14, along with satellite sea ice concentration data, weather station data, and atmospheric reanalysis fields, are used to explore the relationship between the circulation, ice cover, and wind forcing. We find a clear relationship between northeasterly winds along the northwest coast of Alaska and reversed flow along the length of Barrow Canyon and at a mooring site ~ 100 km upstream on the northeast shelf. Atlantic Water is frequently upwelled into the canyon during the fall and winter, but is only able to reach the head of Barrow Canyon after a series of long upwelling events. A pair of empirical orthogonal function (EOF) analyses of ice cover reveal the importance of inflow pathways on the pattern of freeze-up and melt-back, and shed light on the relative influence of sensible heat and wind forcing on polynya formation. An EOF analysis of 25 mooring velocity records reveals a dominant pattern of circulation with coherent flow across the shelf, and a secondary pattern of opposing flow between Barrow Canyon and Bering Strait. These are related to variations in the regional wind field.

1. Introduction

As one of the most productive areas in the global ocean (Grebmeier et al., 2006) and as part of a region currently experiencing a significant decline in sea ice cover (Frey et al., 2015), a better understanding of physical processes in the Chukchi Sea is critical to our understanding of the changing ecosystem dynamics. Timing of melt-back in sea ice controls the seasonal transition from ice algae to phytoplankton as primary producers. An earlier melt-back could shift the ecosystem from a benthic-dominated to a pelagic-dominated regime (Grebmeier et al., 2006; Moore & Stabeno, 2015). Through brine rejection during ice production, the frequency, extent, and duration of polynyas influence the density of winter waters and the depth to which they ventilate the western Arctic (Itoh et al., 2012; Weingartner et al., 1998). The resulting deep convection homogenizes the water column and can resuspend nutrients from the sea floor (Pacini et al., 2019; Pickart et al., 2016). Circulation patterns then control the distribution of nutrients throughout the Chukchi Sea (Pickart et al., 2016), which in turn influences the location and strength of the phytoplankton blooms.

In recent years, a general understanding of the circulation across the Chukchi Sea and regions of likely exchange with the Arctic Basin has emerged (Fig. 1). Flow through Bering Strait is primarily northward, with a higher transport in the summer months (Woodgate et al., 2005a). Northward flow continues across the Chukchi Sea along three major, topographically steered pathways. The coastal pathway, known as the Alaskan Coastal Current (ACC) in the summer, is the most direct route and follows the Alaska coastline across the shelf, draining through Barrow Canyon. The Central Channel pathway flows northward from Bering Strait and subsequently divides into several branches, each eventually turning eastward towards Barrow Canyon (e.g. Pickart et al., 2016). The western pathway is the most circuitous. A portion of this water flows westward through Long Strait into the East Siberian Sea

* Corresponding author.
E-mail address: bovall@marine.rutgers.edu (B. Ovall).
[1] Present address:

https://doi.org/10.1016/j.pocean.2021.102707
Received 7 April 2021; Received in revised form 9 September 2021; Accepted 26 October 2021
Available online 31 October 2021

(Woodgate et al., 2005a,b). The rest flows around the west side of Herald Shoal into Herald Canyon. A bifurcation just north of the canyon diverts some of the flow eastward, which joins the Central Channel pathway near Hanna Shoal. Thus, a large portion of the Bering Strait inflow ends up flowing through Barrow Canyon. However, transit times vary greatly by pathway, ranging from as little as 2–3 months in the coastal pathway (Tian et al., 2021; Weingartner et al., 1998) to 6–8 months for the northernmost branch of the Central Channel pathway (Spall, 2007). Additionally, each pathway experiences intermittent flow reversals associated with local winds, which increase the transit times.

Several studies have explored the connection between local wind forcing and flow reversals within Barrow Canyon (e.g., Itoh et al., 2013; Weingartner et al., 2017; Lin et al., 2019a; Pisareva et al., 2019). Northeasterly wind along the northwest coast of Alaska drives offshore Ekman transport, which in turn leads to upwelling in the canyon. Such wind events are frequent, especially in fall and winter. Continental shelf waves are also thought to play a role in upwelling in this region (Aagaard & Roach, 1990; Danielson et al., 2014). Episodes of upwelling have been known to draw warm, salty Atlantic Water from the deep Arctic Basin, sometimes far onto the shelf (Bourke & Paquette, 1976; Ladd et al., 2016).

Barrow Canyon is an important choke point of the Chukchi circulation that influences the export into the western Arctic. Roughly half of the annual Bering Strait inflow of Pacific Water drains through the canyon (Itoh et al., 2013). It is thus important to understand the factors controlling the circulation and its variability there. For example, what conditions determine which water masses get upwelled through Barrow Canyon? What portion of the Chukchi shelf is influenced by these upwelling events? Pisareva et al. (2019) found that upwelling sometimes delivers denser water to the head of Barrow Canyon and other times delivers lighter water. They noted that much of the difference was due to strong seasonality of the water masses present on the Chukchi Shelf, i.e. the initial water mass. Unlike the findings of Lin et al. (2019b) for the Alaskan Beaufort Slope, Pisareva et al. (2019) found that upwelling of Atlantic Water to the head of Barrow Canyon occurs only infrequently. However, Itoh et al., (2013) report that Atlantic Water is maintained below 150 m at the mouth of Barrow Canyon year round.

While strong northeasterly wind can force a flow reversal (upwelling) in Barrow Canyon, flow is down-canyon under all other wind directions (Lin et al., 2019a). A sea surface height gradient (pressure head) between the Pacific and Arctic Oceans is the primary driver of northward flow through Bering Strait (Coachman & Aagaard, 1966; Woodgate et al., 2005b). The signal of northward flow is largely coherent across the eastern Chukchi Sea (Woodgate et al., 2005b). However, the northward flow is opposed by the mean wind in the region, i.e. northeasterly wind along the northwest coast of Alaska (Pisareva et al., 2019) and northerly wind in Bering Strait (Woodgate et al., 2005b). Woodgate (2018) found that the northward transport through Bering Strait has been increasing in recent years and attributes that trend to an increase in the pressure head. Danielson et al. (2014) propose that the increase in sea surface height on the Bering Sea end of the Strait is due to an eastward shift in the mean position of the Aleutian Low. Danielson et al. (2014) also present evidence of northward propagating shelf waves, which follow the Alaska coastline, and can increase or decrease Bering Strait transport on synoptic time scales, with the sign of the velocity signal depending on the direction of wind that sets up the shelf wave. If flow through Bering Strait and across the Chukchi Sea is primarily driven by the pressure head, but strongly modulated by local winds, do local winds near Bering Strait and near Barrow Canyon always act in concert? What sort of dynamical response might there be if/when they do not?

Although there has only been a slight warming in Bering Strait inflow waters, because of the increased volume transport there has been a significant increase in heat transport through the strait (Woodgate, 2018). Serreze et al. (2016) found heat transport through Bering Strait to be the strongest predictor in timing of both spring ice retreat and fall ice advance. This additional heat flux can also promote sea ice thinning across much of the western Arctic Ocean (Woodgate et al., 2015). How apparent is the effect of seasonal variations in Bering Strait inflow on the spatial pattern of sea ice?

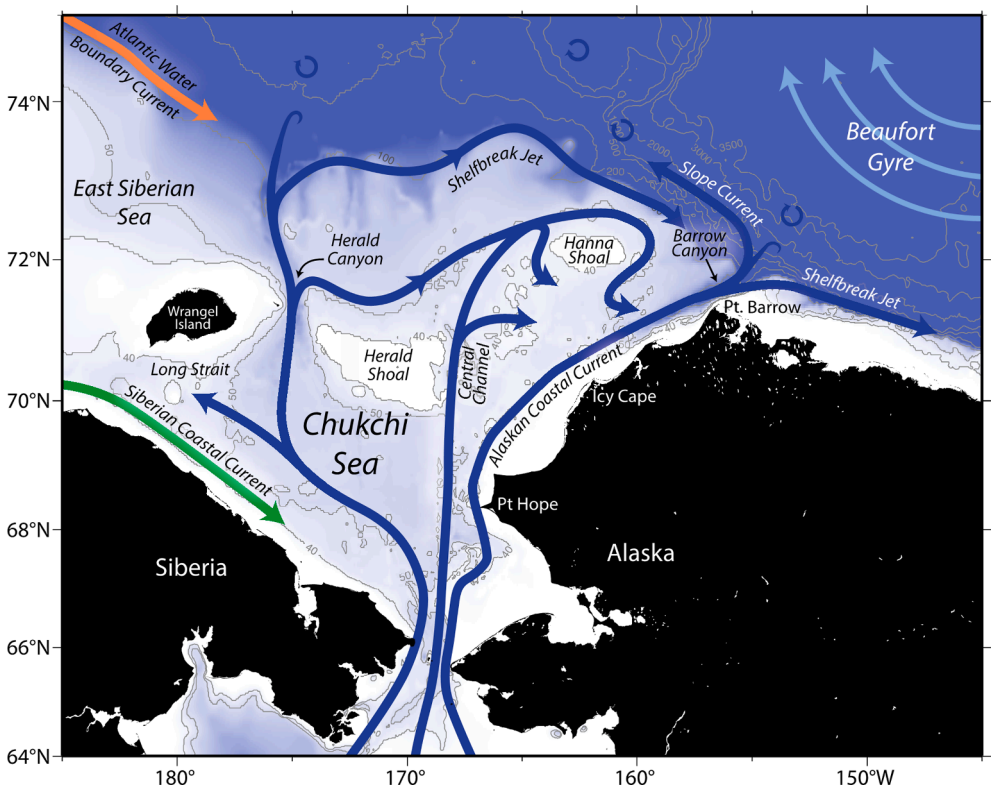

Fig. 1. Circulation schematic of the Chukchi Sea and place names (from Corlett and Pickart, 2017). The bathymetry is from ETOPO2.

Polynyas are a common occurrence in the Arctic. As stated previously, northeasterly winds in the region of Barrow Canyon drive offshore Ekman transport that results in upwelling. Similar wind conditions can also drive offshore ice transport along the northwest coast of Alaska. Such regions of ice divergence along a coastline are known as wind-driven, or latent heat, coastal polynyas (Morales Maqueda et al., 2004). Because the water column in a wind-driven polynya remains at the freezing temperature, new ice is readily formed at the surface. Continued offshore transport of ice makes this type of polynya an ice production zone and contributes to the densification of the water column. Alternatively, sensible heat polynyas are formed when warm ocean waters are introduced to an ice-covered region, melting the existing ice and preventing new ice from forming. The location, extent, and duration of such polynyas are dependent upon the same characteristics of the warm water mass (Morales Maqueda et al., 2004). Hirano et al. (2016, 2018) provide evidence that the recurring polynya in the vicinity of Barrow Canyon is a hybrid latent and sensible heat polynya, influenced by both wind-driven ice divergence and upwelling of warm waters through Barrow Canyon. However, their analysis shows the influence of sensible heat on the polynya is limited to localized areas very near the coastline. Other investigators (e.g. Ladd et al., 2016) have suggested a much larger extent of warm water influence.

In this study we use data from an extensive set of moorings deployed across the Chukchi Sea in 2013–14, from Bering Strait to the western Beaufort Sea, to address some of the above questions. This allows us to explore the coupled nature of the flow across the shelf in relation to the wind forcing and the sea ice concentration. We begin with a description of the data sources utilized and the method used for identifying wind events in Section 2. In Section 3, we give a brief description of the mean flow over the study year. In Section 4, we explore the flow and water mass response in Barrow Canyon to northeasterly wind events. Section 5 investigates spatial patterns in sea ice on regional and local scales and their relationships with potential forcing mechanisms. Shelf-wide circulation patterns and their relationship to regional wind patterns are explored in Section 6. A summary of our results is presented in Section 7.

2. Data and methods

2.1. Moorings

In 2013, there was an extraordinary number of moorings deployed in the northeastern Chukchi Sea as a result of projects conducted by multiple institutions. Here we use data from 27 moorings: 22 from the northeastern Chukchi shelf and adjacent slope, one from the Beaufort slope, one from the southern Chukchi shelf, and three from Bering Strait (Table 1; Fig. 2). Although the exact dates of deployment varied by project, seasonal access to the region limits deployment and retrieval of moorings to summer/early-fall, which resulted in fairly consistent coverage at all mooring sites.

For our analysis, we consider only data during the 12-month period from Oct 2013 through Sep 2014, which provides the most complete data coverage (Fig. 3). This choice of dates restricts missing data at most

Table 1
Mooring descriptions.

ID	Lat (°N)	Lon (°W)	Water Depth (m)	Deployment Dates (mm/dd/yyyy)	ADCP			MicroCAT/ SeaCAT		Institution[a]
					Range (m)	Sample Int. (h)	Vertical Res. (m)	Depth (m)	Sample Int. (h)	
A2[b,c]	65°47′	168°34′	54	07/06/2013–07/01/2014	1–39	0.5	2	50	1	UW/APL
				07/03/2014–07/04/2015				50	1	
				07/03/2014–08/07/2014	1–39	0.5	2			
				08/07/2014–07/04/2015	1–37	1	4			
A3[b]	66°20′	168°57′	56	07/05/2013–07/02/2014	1–39	0.5	2	45	1	UW/APL
				07/02/2014–07/03/2015	1–39	0.5	2	43	1	
A4[b]	65°45′	168°16′	47	07/06/2013–07/01/2014	1–33	0.5	2	40	1	UW/APL
				07/03/2014–07/03/2015	1–33	0.5	2	40	1	
BCE	71°40′	155°0′	107	09/06/2013–09/11/2014	3–75	2	4	93	1	JAMSTEC
BCH	71°19′	157°9′	60	07/24/2013–07/23/2014	–	–	–	56	1	JAMSTEC
BCW	71°48′	157°21′	171	09/07/2013–09/11/2014	2–138	2	4	81	1	JAMSTEC
BC2	70°55′	159°56′	52	09/11/2013–09/23/2014	3–46	0.5	1	51	0.25	UAF
BS3	71°24′	152°3′	147	10/21/2013–07/17/2014	10–115	1	5	40	12	WHOI
Bu	71°14′	163°17′	46	08/01/2013–08/05/2014	17, 35	0.25	–	38	0.25	ASL
Cj	71°10′	166°45′	47	07/31/2013–07/31/2014	21, 35	0.25	–	40	0.25	ASL
C1	70°50′	163°7′	44	08/27/2013–09/25/2014	4–28	1	4	40	1	PMEL
C2	71°13′	164°17′	43	08/27/2013–09/26/2014	7–37	1	2	39	1	PMEL
C5	71°12′	158°0′	53	08/31/2013–09/29/2014	5–33	1	4	44	1	PMEL
C6	71°47′	161°52′	42	08/28/2013–10/04/2014	13–39	1	2	39	1	PMEL
C7	72°25′	161°36′	42	08/29/2013–10/02/2014	4–32	1	2	41	1	PMEL
CS2	72°18′	157°44′	102	10/12/2013–09/22/2014	16–81	1	5	90	0.25	WHOI
CS3	72°20′	157°27′	163	10/13/2013–09/22/2014	22–132	1	10	41	6	WHOI
CS4	72°23′	157°9′	249	10/13/2013–09/22/2014	22–222	1	10	54	6	WHOI
CS5	72°26′	156°50′	357	10/13/2013–09/22/2014	31–331	1	10	44	6	WHOI
CT	72°13′	166°58′	48	10/09/2013–07/10/2014	8–38	1	5	46	0.25	WHOI
FM1	72°16′	158°2′	67	10/25/2013–09/21/2014	13–53	1	5	61	0.25	UAF
NE40	72°7′	160°30′	41	09/09/2013–09/18/2014	3–37	0.5	1	37	0.25	UAF
NE50	72°10	159°7′	50	09/09/2013–09/18/2014	4–46	0.5	1	46	0.25	UAF
NE60	72°11′	158°33′	57	09/09/2013–09/18/2014	5–53	0.5	1	53	0.25	UAF
NW40	72°17′	163°32′	41	09/10/2013–09/20/2014	3–37	0.5	1	38	0.25	UAF
NW50	72°32′	164°6′	51	09/09/2013–06/16/2014	4–47	0.5	1	47	0.25	UAF
SCH	68°2′	168°50′	61	07/20/2013–07/19/2014	–	–	–	53	1	JAMSTEC

[a] University of Washington Applied Physics Laboratory (UW/APL), Japan Agency for Marine-Earth Science and Technology (JAMSTEC), University of Alaska Fairbanks (UAF), ASL Environmental Sciences, Inc. (ASL), National Oceanic and Atmospheric Administration Pacific Marine Environmental Laboratory (PMEL), Woods Hole Oceanographic Institution (WHOI)

[b] Two deployment years were spliced together in order to cover the entire study year, resulting in a small gap at turnaround. ADCPs contained significant errors in the surface bins, so those levels were omitted from the analysis (above 8 m at A2 and above 7 m at A3 and A4).

[c] While the MicroCAT operated without incident during the 2014 deployment, the ADCP experienced an error about one month in, which caused it to reset to factory defaults. Portion with 4 m vertical resolution was interpolated to 2 m resolution.

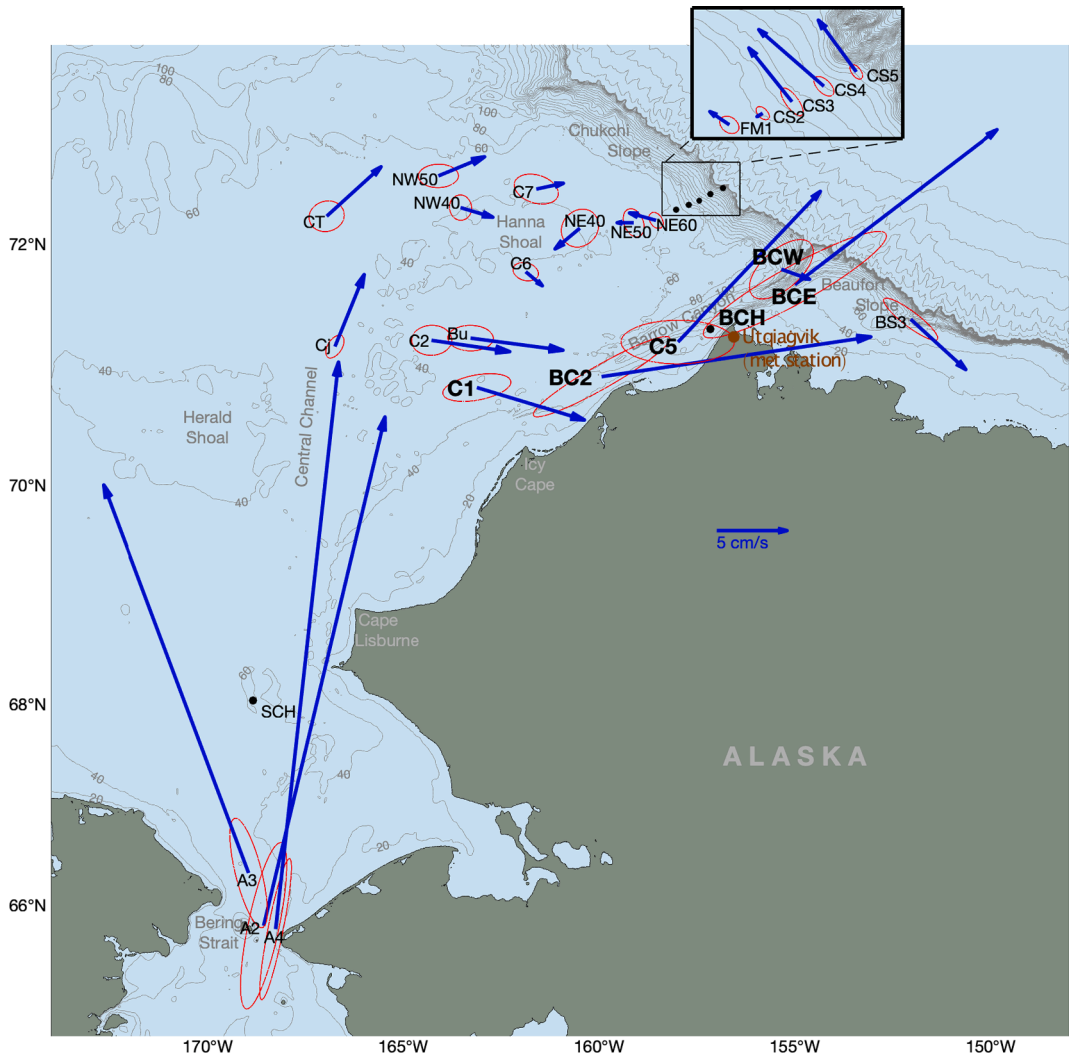

Fig. 2. Mean depth-averaged velocity vectors for the study year (Oct 2013 – Sep 2014) with standard error ellipses. Bold lettering indicates moorings within the coastal pathway. Bathymetry contours at 20 m intervals to 500 m, then 500 m intervals. Note that no velocity data were collected at moorings BCH and SCH. The location of the meteorological station in Utqiaġvik is marked in brown.

moorings to a few weeks or less at the beginning and/or end of the year. A few moorings have a longer gap. CT had a total deployment period of 9 months, with most of the gap occurring at the end of our year. Cj, Bu, BS3, BCH, and SCH were retrieved in late July/early August. The acoustic Doppler current profiler (ADCP) at NW50 and the MicroCAT at CS5 both failed in mid-June. For the Bering Strait moorings, A2, A3, and A4, we spliced together two separate deployments so there is a small gap at each mooring turnaround.

All of the moorings were equipped with SeaBird MicroCATs (SBE 37) or SeaCATs (SBE 16 or SBE 19) measuring temperature, conductivity, and pressure near the bottom. With the exceptions of SCH and BCH, all moorings were equipped with bottom-mounted, upward-facing Teledyne RDI 300 or 600 kHz ADCPs. The velocity timeseries were de-tided using the T_TIDE harmonic analysis toolbox (Pawlowicz et al., 2002), although the tides are much weaker than the signals of interest. The largest tidal amplitudes observed were 4 cm s^{-1}, although most were 1–2 cm s^{-1}. Mooring Cj had the largest tidal amplitude relative to variability in the full velocity record. Here, the M2 tide had an amplitude of 3.5 m s^{-1} while the standard deviation in velocity was 7.2 m s^{-1}. The rest of the moorings had lower tidal amplitudes and/or higher standard deviations in velocity. Gaps in the timeseries were filled in using two-dimensional Laplacian-spline interpolation. The vast majority of these gaps consisted of a few hours and/or covered less than 10% of the measured water column. The most extensive set of gaps occurred at C6 where there was a 30-day period in the mid-winter when readings throughout the top 1/3 of the water column were intermittent. However, given the strongly barotropic nature of the flow, these could reasonably be interpolated.

Sample intervals varied by mooring (Table 1). All mooring data were interpolated and/or subsampled, as appropriate, to obtain hourly data. For all analyses of water velocity, the depth-averaged flow (over the depth-range covered by the respective ADCP) is used. Across the study region, the flow is largely barotropic. Because most mooring locations exhibit little variation of flow speed and direction with depth, even though there is some inconsistency in the proportion of the water column covered by each ADCP, the depth-averaged velocities are considered representative of the full water column. Exceptions to that occur east of Hanna Shoal (NE40, NE50, and NE60), across the Chukchi Slope (CS2-5), and on the Beaufort Slope (BS3). East of Hanna Shoal, the surface layer is baroclinic and flow direction can vary greatly between surface and bottom layers. Along the Chukchi and Beaufort Slopes, shelfbreak jets and the Chukchi Slope Current generally manifest as a core of flow in the opposite direction of the waters above or below them. For these locations, the depth-averaged velocity is still used to illustrate that variability at these locations coincides with that of the large-scale flow patterns over the rest of the study region (as discussed in section

Fig. 3. Data coverage at each mooring over the study year, defined as 1 Oct 2013 – 30 Sep 2014. Purple lines indicate dates for velocity data and blue lines indicate dates for temperature/salinity/pressure data. (For interpretation of the references to color in this figure legend, the reader is referred to the web version of this article.)

6), but the reader should be aware that the vertical structure is not represented. For discussions of vertical structure at these locations, the reader is referred to Fang et al. (2020) and Tian et al. (2021) for the area east of Hanna Shoal, Li et al., (2019) for the Chukchi Slope, and Nikolopoulos et al. (2009) for the Beaufort Slope.

2.2. Wind conditions

For broad-scale wind conditions, we used the 10-m winds from the ERA5 reanalysis (Hersbach et al., 2020) from the European Center for Medium-Range Weather Forecasts (ECMWF, https://www.ecmwf.int/). ERA5 is the fifth-generation product, an updated version of ERA-Interim, with higher spatial and temporal resolutions of 0.25° and 1 hr, respectively. Here we use 3-hourly resolution.

To identify wind events that potentially drive upwelling in Barrow Canyon, we use the wind record from the meteorological station at Utqiaġvik, AK (formerly Barrow, AK). The hourly wind data for the study period were obtained from the National Climate Data Center of the National Oceanic and Atmospheric Administration (http://www.ncdc.noaa.gov/). The data have been subsequently quality controlled by removing outliers and interpolating over small gaps (see Pickart et al., 2013, for details) , and are widely used in studies of the northern Chukchi Sea and western Alaskan Beaufort Sea (e.g., Lin et al., 2016; Lin et al., 2019b). For the full record (1941–2017), the mean wind speed was 2.06 m s^{-1} directed along 257°T. For the dates of the study year the mean wind speed was 1.64 m s^{-1} along 256°T. Using 230°T as the positive along-coast direction in the vicinity of Barrow Canyon, a minimum wind speed threshold was chosen which best captured discrete wind events (i.e., time periods when northeasterly wind was visibly stronger than background levels). We identified events as having an along-coast wind speed greater than 4 m s^{-1} sustained for at least 24 h. Once the 24-hour minimum is met, a reduction of along-coast wind speed for up to 12 h is permitted within the event. Thus, the beginning of an event is the first hour that along-coast wind speed exceeds 4 m s^{-1}, the duration is the time period during which all criteria are met, and the end of the event is the last hour that wind speed exceeds 4 m s^{-1} (after which there is more than 12 h of reduced wind speeds).

Using these criteria, we identified 23 wind events over the course of the year (Table 2). However, these thresholds allow for significant variability in wind direction. Lin et al., (2019a) found that flow reversals in Barrow Canyon only occur under northeasterly winds, but a strong east-southeasterly wind can still have an along-coast component above 4 m s^{-1}. For the purposes of evaluating the water column response to northeasterly wind events, we use the six events with the clearest signal

Table 2
Wind event details. Asterisks indicate the clear northeasterly events used for the upwelling response analysis. Bold lettering indicates events occurring during the full-ice period.

Designation	Start (2013)	End (2014)	Duration (hrs)	Mean Wind Speed (m s^{-1})	Max Wind Speed (m s^{-1})
E1	8 Oct	10 Oct	45	7.9	14.9
E2	13 Oct	14 Oct	27	7.5	10.1
E3*	19 Oct	21 Oct	42	7.6	10.6
E4*	22 Nov	25 Nov	66	7.6	12.5
E5	5 Dec	7 Dec	45	7.8	10.1
E6	8 Dec	10 Dec	42	7.4	12.2
E7*	**21 Dec**	**22 Dec**	**33**	**7.8**	**10.6**
E8	**27 Dec**	**9 Jan**	**306**	**7.7**	**15.0**
E9	**17 Jan**	**29 Jan**	**280**	**7.8**	**14.2**
E10*	**14 Feb**	**18 Feb**	**99**	**5.9**	**8.9**
E11	**22 Feb**	**24 Feb**	**43**	**7.2**	**9.2**
E12	**26 Feb**	**28 Feb**	**53**	**7.3**	**11.2**
E13*	**11 Mar**	**12 Mar**	**26**	**6.2**	**7.9**
E14	**13 Mar**	**15 Mar**	**54**	**5.6**	**8.6**
E15	**18 Apr**	**23 Apr**	**103**	**5.0**	**8.8**
E16	**27 Apr**	**29 Apr**	**51**	**7.8**	**10.9**
E17*	**27 May**	**2 Jun**	**147**	**8.7**	**12.7**
E18	**8 Jun**	**12 Jun**	**89**	**5.0**	**7.4**
E19	18 Jun	23 Jun	109	6.8	9.7
E20	26 Jun	28 Jun	56	5.7	6.9
E21	7 Jul	11 Jul	92	6.4	8.9
E22	7 Aug	17 Aug	253	8.7	14.7
E23	9 Sep	21 Sep	294	6.8	10.7

of sustained northeasterly wind. These were events with a clear beginning and end, which maintained a northeasterly wind direction throughout. The purpose of being selective in these events was to get a clear picture of the water column response to northeasterly winds in the absence of other influencing factors. Wind events identified by local winds are labeled E1-E23 (Table 2). The six clear northeasterly events are E3, E4, E7, E10, E13, and E17 (designated with an asterisk in Table 2).

2.3. Ice concentration

The daily ice concentration data used in this study are provided by the Remote Sensing of Sea Ice Research Group at the University of Bremen (https://seaice.uni-bremen.de/). The data are obtained by applying the ARTIST (Arctic Radiation and Turbulence Interaction STudy) Sea Ice algorithm (Spreen et al., 2008) to the original measurements of the new Advanced Microwave Scanning Radiometer (AMSR2) launched in 2012 (Beitsch et al., 2014), as the successor of AMSR-E. The resolution of the product is 3.125 km in our study region.

3. Mean shelf-wide flow

The depth-averaged mean flow for the study year shows many of the features observed in previous studies (Fig. 2; see also Tian et al. (2021) who analyzed the same set of moorings). There is strong inflow through Bering Strait (A2-A4, mean 29.5–40.6 cm s^{-1}), and evidence of the two pathways on the eastern side of the Chukchi Sea. The coastal pathway (bold-lettered mooring locations) corresponds to high velocities as water drains from the shelf via Barrow Canyon (mean at BC2 is 19.4 cm s^{-1}). The relatively low mean velocity at BCW (2.1 cm s^{-1}) is due to the fact that flow out of the canyon at this location ranges from northwestward to southeastward and much of this variability cancels out in the mean. The Central Channel pathway bifurcates in the vicinity of Cj (mean 5.5 cm s^{-1}): one branch flows eastward (C2 and Bu) towards Barrow Canyon, and the other branch continues northward towards CT before being diverted eastward around the north side of Hanna Shoal (means near Hanna Shoal range from 1.2 to 3.6 cm s^{-1}). The mean southeastward flow at C6 is consistent with either cyclonic flow around the south side of Hanna Shoal or a retroflection towards Barrow Canyon after anticyclonic flow around the north side of Hanna Shoal. The eastward flowing Beaufort Shelfbreak Jet is seen at BS3 (mean 5.3 cm s^{-1}), and the westward flowing Chukchi Slope Current is evident at CS3-5 (mean 5.3–7.0 cm s^{-1}). There is a hint of the eastward-flowing Chukchi Shelfbreak Jet at CS2; however, the jet is bottom intensified with oppositely directed flow in the surface layer, resulting in a depth-averaged mean flow close to zero (Li et al., 2019).

4. Upwelling response in Barrow Canyon

4.1. Composite water column response

The duration of the six northeasterly wind events (see section 2.2 for details on selection criteria), varied from 26 h to 147 h, with mean along-coast wind speeds of 5.9 – 8.7 m s^{-1}. By normalizing time, with $t = 0$ and $t = 1$ corresponding to the first and last hours that wind speed thresholds were met (refer to section 2.2), we created a composite timeseries of wind speed for the six events (Fig. 4a). We then created corresponding composites of the depth-averaged velocity (Fig. 4b-f) at the five mooring sites along the coastal pathway that had ADCPs (four in Barrow Canyon and one upstream). The moorings along the coastal pathway are labeled with bold lettering in Fig. 2, including mooring BCH which has no velocity data. The composites show a strong reversal of direction from the mean flow that occurs nearly simultaneously with the change in wind speed. For most of the moorings in Barrow Canyon, the reversed flow is up-canyon along the canyon axis. The flow at C5 appears anomalous, but is in fact in the up-canyon direction along the local bathymetry at that site. The flow response at C1 on the shelf, ~100 km upstream of the canyon, illustrates the tightly coupled nature of upstream flow and the flow in Barrow Canyon. Over the entire year, the principal component of velocity (i.e., the component along the axis of maximum variance) at C1 and BC2 (at the head of the canyon) are highly correlated (r = 0.87). As seen in the composites, the water column response at C1 occurs just as quickly as at BC2.

The strong reversal of flow seen in the composites at each mooring site is representative of the water column response during individual wind events. The pre-event composite (gray vectors preceding $t = 0$) is included to illustrate the distinct change in flow that occurs with the onset of northeasterly winds. However, pre-event conditions are highly variable, ranging from strong down-canyon (or other non-reversed direction) flow, to weak flow, to strong flow in the reversed direction. The

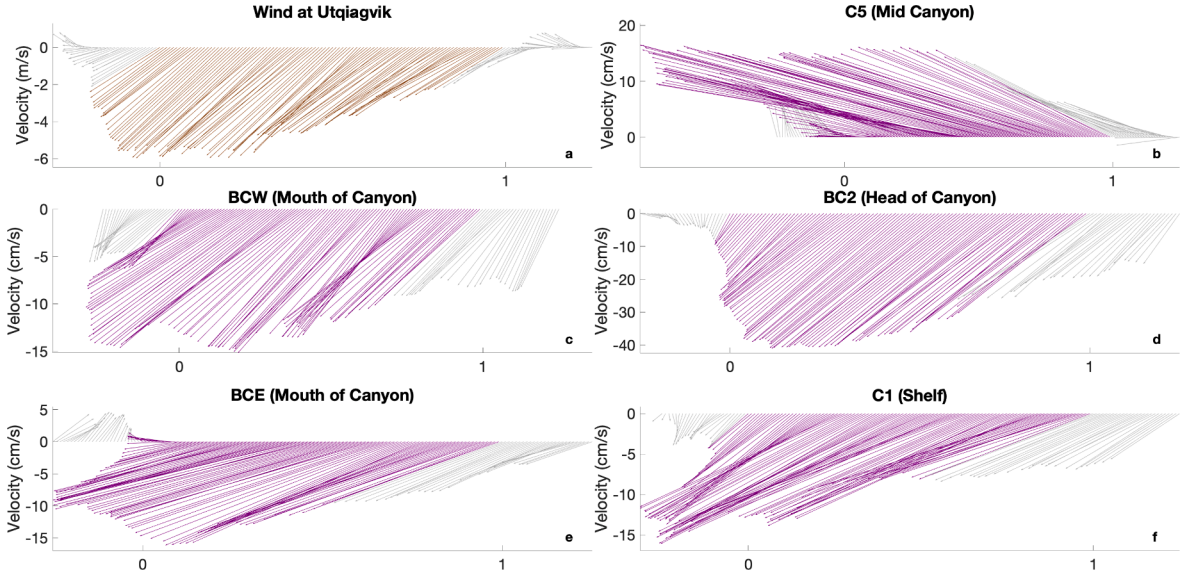

Fig. 4. Composites constructed using normalized time (see text for details). Colored vectors represent velocities over the wind event duration. Gray vectors represent velocities preceding and following the event, each over a duration of 25% of the event length. (a) Wind velocity at Utqiaġvik met. station. (b-f) Depth-averaged velocity at moorings in and upstream of Barrow Canyon.

pre-event portion of the composites should not be taken as representative of background conditions. The composites at all five mooring sites show a lag in the relaxation of flow after the end of the event (gray vectors following $t = 1$). However, this is not true for all of the individual events.

4.2. Velocity response to wind event strength

Next, we assess the relationship between the strength of a wind event and the strength of the depth-averaged flow response. To quantify the strength of a wind event, we calculated the cumulative Ekman transport over the duration of each event:

$$CET = \int_{t_s}^{t_e} \frac{\tau_a(t)}{f\rho_0} dt,$$

where τ_a is the along-coast component of the wind stress (following Large and Pond, 1981), ρ_0 is a representative water density for the region, f is the Coriolis parameter, t_s and t_e correspond to the start and end times of the event (as described in section 2.2). Thus, cumulative Ekman transport takes into account both the magnitude and the duration of the event.

Similarly, the strength of the flow response was calculated as a cumulative velocity anomaly from the initial condition:

$$CVA = \frac{1}{H}\int_{t_s}^{t_e}\int_{bot}^{top} (v(z,t) - v_0(z))dzdt$$

where v_0 is the velocity at the beginning of the event, v is the velocity at each time step, and H is the total depth over which the velocity is measured. Since several of the mooring sites do not exhibit rectilinear flow (i.e., 180° offset between reversed and non-reversed directions), velocity here is simply categorized as negative when in the general direction of the mean flow and positive when in a direction that would collectively lead to a reversed flow path, and the full magnitude of velocity is used. This allows for a comparison of flow reversal for mooring sites with a variable non-reversed flow direction. This categorization of flow is also beneficial at C1, where the mean flow is largely eastward, but the reversed flow often has a significant southward component. Calculating the response as an anomaly from the initial condition allows for events that start with strong down-canyon flow to be compared with events that start when there is already up-canyon flow. Calculating CVA as a depth-averaged velocity allows for comparison of sites with different depths.

Using CET to quantify wind event strength and CVA to quantify water column response, we find that, overall, stronger events induce a stronger response (Fig. 5, where the wind event strength is plotted on a log scale). It must be kept in mind, however, that this is based on the six events with the clearest signal of sustained northeasterly winds. When considering all 23 events (not shown), the pattern is less clear. While there is still a general increase in response strength with increasing wind event strength, there is significantly more scatter about this trend.

There is also an apparent difference in velocity response by mooring site. One would expect an Ekman-related response to diminish with distance from the coast. Indeed the moorings farthest from the coast (BCW and C1) consistently have the lowest response strength (except for E10). However, the geometry of the canyon and a simple conservation of mass argument may also provide sufficient explanation. BCW and C1 have the deepest and widest channels, respectively, allowing the response to be distributed over a larger area. BC2 and C5 generally have the highest response strength. Both of these moorings are located where the canyon narrows (in a reversed-flow perspective), which would concentrate the response. E10 has an anomalously large response at BC2, C1, and BCW. At these sites, strong up-canyon flow continues for more than two days after the winds have subsided at Utqiaġvik, with BC2 being the last site to resume down-canyon flow. The delay for upwelling to relax as the winds decrease could explain the anomalous response at these locations.

During the course of the year, some of the upwelling events begin prior to the onset of northeasterly winds at Utqiaġvik (one upwelling event begins a full week prior), some of the events continue after winds subside, and two weak upwelling events occur in the absence of northeasterly winds. This and the scatter in the relationship between event strength and velocity response suggests the influence of other forcing, perhaps related to propagating shelf waves. Using an idealized numerical model, Danielson et al. (2014) show that winds over the Bering Sea can initiate shelf waves that propagate northward along the Alaska

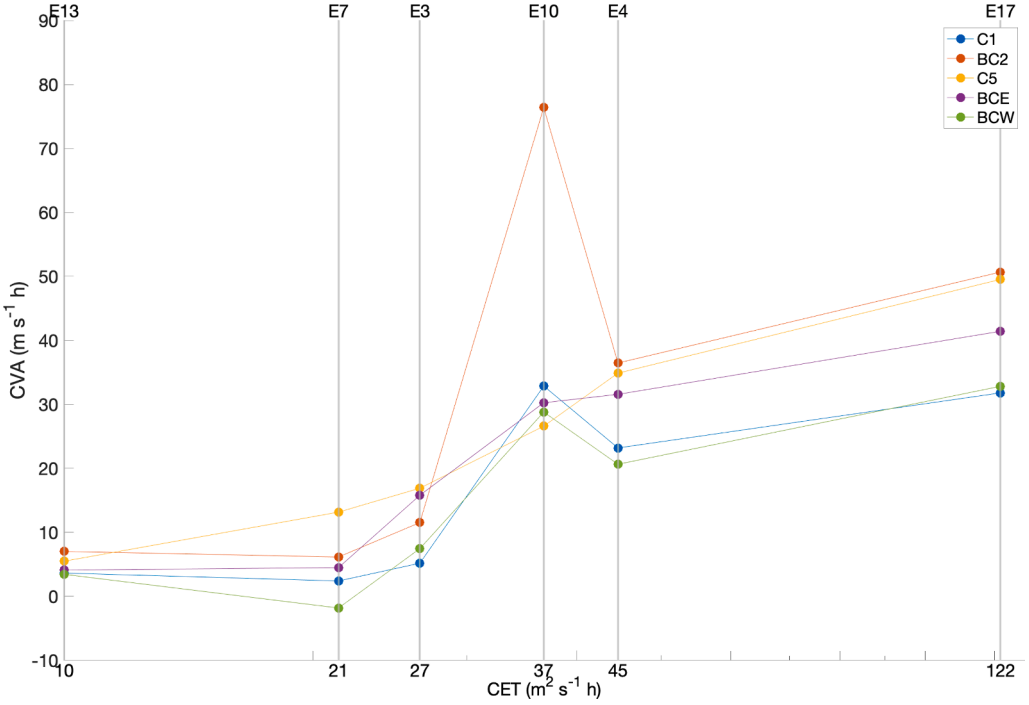

Fig. 5. Comparison of wind event strength (CET) to velocity response (CVA) at each mooring along the coastal pathway. CET is plotted on a log scale.

coastline and can induce a velocity response in both Bering Strait and Barrow Canyon. In a generalized linear model exploring the relationship between reanalysis wind fields and a mooring array at the head of Barrow Canyon (which included mooring site BC2 from the current study, although during an earlier year), Danielson et al. (2014) find that remote winds account for a significant proportion of the transport. We do see potential indicators for a role of propagating shelf waves in our analysis, although it is not a dominant effect. This is being addressed in an ongoing study.

4.3. Water mass response to upwelling

As mentioned earlier, much of the water that flows across the Chukchi Sea eventually drains through Barrow Canyon. There is significant interannual variability in water mass properties, but we adopt a generalized classification of water masses based on potential temperature and salinity ranges used in previous studies (e.g., Pickart et al., 2019; Pisareva et al., 2019). In the spring and summer, the inflow through Bering Strait is relatively warm and fresh. The two Pacific-origin summer water masses are Bering Summer Water [BSW] and Alaskan Coastal Water [ACW], with ACW being warmest and freshest (Table 3). During the cold months of the year, Newly Ventilated Winter Water [NVWW] is advected through Bering Strait. This water mass is close to the freezing point and can be further transformed locally on the Chukchi shelf via convective overturning in polynyas and leads (Weingartner et al., 1998; Pickart et al., 2016; Pacini et al., 2019). NVWW eventually warms to become Remnant Winter Water [RWW] due to solar heating and/or mixing with summer waters (e.g. Gong & Pickart, 2016). RWW constitutes the cold halocline of the interior western Arctic (Woodgate, 2012), where it is more generally referred to as Pacific Winter Water. Finally, cold and very fresh water is classified as Melt Water [MW], which can also include river runoff.

Due to a variety of factors, including differences in the transit times for each of the flow paths and the melt/freeze cycle of the pack ice, the seasonality of water masses in Barrow Canyon is not the same as in Bering Strait (e.g. Tian et al., 2021). For example, NVWW can be found in the canyon in late-summer, having arrived via the central pathway and around Hanna Shoal (Fang et al., 2020; Pickart et al., 2019). Barrow Canyon also sees intermittent appearances of Atlantic Water [AW] associated with upwelling events. Bear in mind, however, that the hydrographic sensors on the moorings are situated near the bottom and therefore will not detect lighter summer waters if they are confined to the surface layer.

While there was a clear relationship between wind event strength and velocity response, there is no apparent connection between event strength and the properties of the upwelled water. Our measurements reveal that some upwelling events result in a density increase at the head of Barrow Canyon and others result in a density decrease, as observed by Pisareva et al. (2019), but we also find that many upwelling events are associated with little density change. Overall, the relative density change is largely dependent on the water mass present at the head of the canyon at the start of an event, which is seasonally varying. For example, at the start of E3 there is light BSW at the head of the canyon (Fig. 6a). This relatively weak wind event (refer to Fig. 5) results in the upwelling of RWW to BC2. The much stronger E17 starts with NVWW at the head of the canyon and brings only more NVWW to BC2 (Fig. 6b). The final water mass has a lower density than the initial water mass. The density of the final water mass for both events is near 26.0 kg m^{-3} and the magnitude of the density change is larger for the weaker event.

Table 3
Water mass definitions.

Water Mass	Abbreviation	Salinity Range	Potential Temperature Range (°C)
Melt Water	MW	0 – 30	any
		30 – 31.5	<0
Alaskan Coastal Water	ACW	30 – 32	> 3
Bering Summer Water	BSW	30 – 33.6	0–3
		32 – 33.6	> 3
Newly Ventilated Winter Water	NVWW	> 31.5	< −1.6
Remnant Winter Water	RWW	31.5 – 33.6	−1.6 to 0
		> 33.6	−1.6 to −1.26
Atlantic Water	AW	> 33.6	> −1.26

The absence of a direct link between wind events and water properties in Barrow Canyon motivates us to explore the water mass signatures over the entire year (Fig. 7). Because of the multiple moorings available, we can get a sense of the progression of water masses along the length of the canyon. Pickart et al. (2019) found that upwelling water masses bank up against the eastern flank of Barrow Canyon, which could be related to the higher velocity responses we found at BCE, C5, and BC2. We also find that water masses present at BCW (on the western side of the canyon mouth) have little relationship to the water masses present at the other moorings along the canyon. For this reason, we focus on the mooring sites on the eastern side of Barrow Canyon. The most obvious feature is a strong seasonality, which matches well with that described by previous studies except that summer waters were late to arrive in 2014 (although they may have been present earlier at shallower depths). Summer waters are present from Oct-Nov 2013 and return Sep 2014, while NVWW occupies the canyon from Dec through mid-Jul. With the exception of brief appearances at BCE and BCH, AW is not measured at all in summer and is only present episodically in late fall and winter. During each of these episodes, AW progresses from the mouth of the canyon towards the head and coincides with reversed flow at the head of Barrow Canyon (black bars at top of Fig. 7). Each time the AW is preceded by RWW (recall that cold halocline water in the interior of the Arctic Basin also fits within this definition). AW only reaches C1, upstream of Barrow Canyon, during one upwelling event (late Jan). Because AW was only detected for a total of 13 h, it simply appears as a dark line in the figure. With four years of data, Ladd et al. (2016) recorded 5 upwelling events which resulted in AW at C1, so it is indeed uncommon. It is worth noting that, in many cases, upwelled water masses reach BCH before BCE (note blocks of AW in Fig. 7). The reason for this is unclear, but may simply reflect that the water mass shoals along the length of the canyon more readily than at the mouth of the canyon. The combination of flow over shoaling bathymetry and through a narrowing channel would cause the lifting of isopycnals along the canyon to outpace their lifting at the mouth.

Comparing water masses to the direction of flow at the head of Barrow Canyon (BC2, see Fig. 7) allows us to identify patterns associated with upwelling events regardless of whether or not they are associated with northeasterly wind at Utqiaġvik. We see that AW only reaches the head of Barrow Canyon (BC2) in the winter, after a series of long upwelling events. From mid-December through the beginning of February, there isn't sufficient time between upwelling events for the RWW to drain completely from the canyon. Over the first half of February, NVWW once again flushes out the canyon. The next long upwelling event, in mid-February, results in a swift return of AW to the canyon, suggesting that water from the previous upwelling event may not have fully receded into the basin. Nikolopoulos et al. (2009) found that the interface between Pacific Winter Water and AW in the Arctic Basin is higher in the water column in late-fall and winter, which could also affect the availability of AW for upwelling into Barrow Canyon.

5. Patterns in ice cover

5.1. Seasonality of regional ice cover

To assess the relationship between ice cover and the circulation across the eastern Chukchi shelf, we first performed an empirical orthogonal function (EOF) analysis of the regional ice cover extending from 174°W to 147°W and 65°N to 74°N (roughly the domain of Fig. 2).

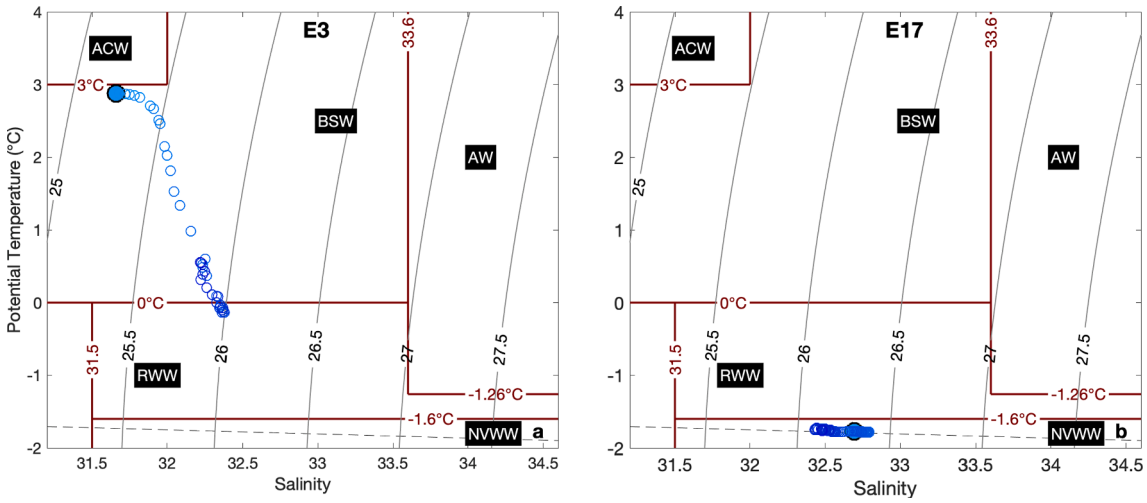

Fig. 6. Water properties at mooring BC2 over the course of wind events (a) E3 and (b) E17. The large filled circles indicate the initial water properties. Smaller unfilled circles represent the properties at each time step. Darkness of color indicates passage of time. Dark red lines delineate water mass boundaries as defined in Table 3. (For interpretation of the references to color in this figure legend, the reader is referred to the web version of this article.)

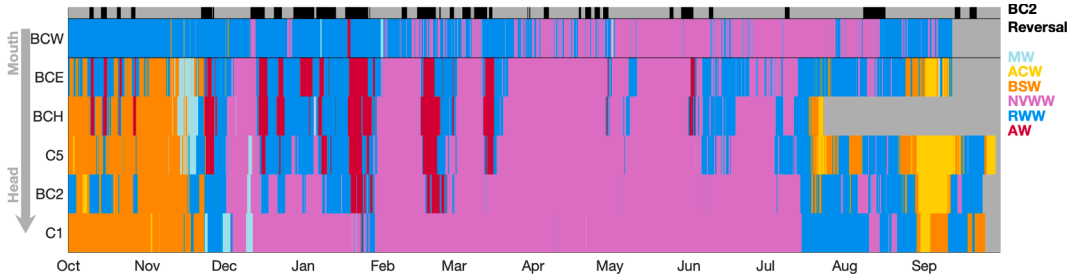

Fig. 7. Timeseries of water masses present along Barrow Canyon and just upstream at C1 (coastal pathway). Water mass abbreviations are defined in Table 3. Black bars at the top indicate times when the flow is up-canyon at BC2.

The year-long mean ice concentration for 2013–14 is shown in Fig. 8a. As one would expect, there is an overall gradient associated with higher mean ice concentrations in the north and lower mean ice concentrations in the south. Also visible in the mean is a signature of the three main inflow pathways across the Chukchi Sea. These appear as tongues of lower mean concentration along the northwest coast of Alaska,

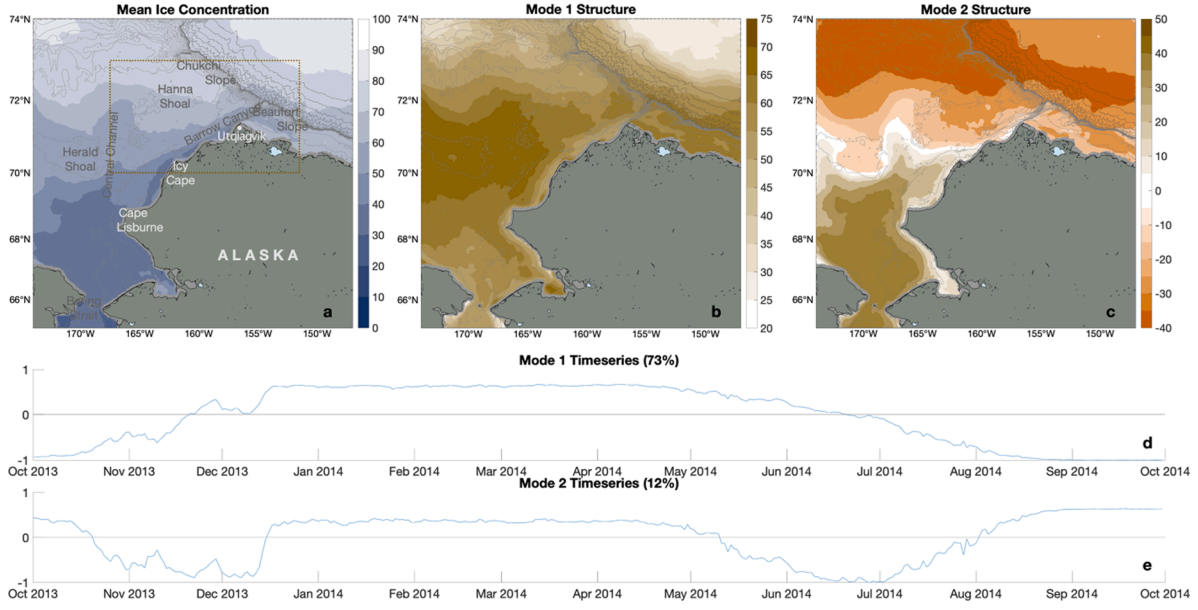

Fig. 8. Large-scale EOF of ice cover over the study year. (a) Mean ice concentration. (b) Structure function for mode 1. (c) Structure function for mode 2. (d) Modal amplitude timeseries for mode 1. (e) Modal amplitude timeseries for mode 2. The box in (a) delimits the smaller spatial domain represented in the local ice EOF below.

extending northward in Central Channel, and extending northwestward towards Herald Canyon (out of the domain). There are also isolated patches of low mean ice concentration adjacent to the northwest coast of Alaska, which reflect the occurrence of polynyas.

We first provide a brief overview of the two primary modes, followed by more detailed discussion of each. Mode 1 (Fig. 8b,d), which explains 73% of the variance, depicts the entire domain varying with the same sign as it transitions from the negative state to the positive state in fall and then back to the negative state in spring. By contrast, mode 2 (Fig. 8c), which accounts for 12% of the variance, depicts the northern and southern portions of the domain varying with opposite signs. The mode 2 amplitude timeseries (Fig. 8e) reveals that this mode has background conditions in the positive state and enters the negative state during the same time periods that mode 1 transitions between states. These fall and spring time periods correspond to the periods of freeze-up and melt-back seen in the full record. We, therefore, conclude that mode 1 represents the transition between summer and winter conditions and mode 2 represents the pattern of variability during the fall freeze-up and spring melt-back periods.

5.1.1. Mode 1: Summer and winter states

Over the course of the year, ice cover ranges from completely open water across the domain in summer to completely ice covered, with concentrations near 100%, across the domain in winter. The modal amplitude timeseries for mode 1 (Fig. 8d) illustrates this transition, with the maximum negative state describing summer conditions and the maximum positive state describing winter conditions. The structure of this mode (Fig. 8b) shows the entire domain varying with the same sign. All points are above their mean in winter and below their mean in summer. The middle of the domain (roughly 69°N to 72°N) shows the greatest variance, while the northern region (ice covered much of the year) and southern region (open water much of the year) show less. There is little evidence of the inflow pathways in the structure of this mode.

5.1.2. Mode 2: Freeze-up and melt-back

The mode 2 structure (Fig. 8c) is oppositely signed in the northern and southern regions of the domain. The positive state has the effect of making the ice concentration across the domain more uniform, while the negative state has the opposite effect, increasing the north–south concentration gradient. Notably, the mode 2 structure shows the signature of the inflow pathways. When added to the mean, the structure function diminishes this signature during summer and winter, and enhances it during freeze-up and melt-back (not shown). Similar magnitudes of the mode 2 timeseries during freeze-up and melt-back show that the pattern is equally evident in both time periods. The ability of these pathways to enhance melt-back in spring is commonly noted (e.g., Spall, 2007; Woodgate et al., 2010), while our analysis highlights the fact that these pathways can also act to delay freeze-up in the fall.

Both modes portray melt-back as a smooth transition occurring over approximately three months. The mode 1 timeseries shows melt-back as a linear transition from full ice to open water. The mode 2 timeseries shows it as a transition from uniform conditions to a strong north–south concentration gradient and back to uniform conditions. With the exception of 20–23 May, there is consistent northward flow through Bering Strait over this time period and the inflow pathways are apparent in the mode 2 pattern of melt-back. The freeze-up process is less smooth, but only takes about two months. Mode 1 shows it as occurring in several steps. Mode 2 shows it as a sharp transition from uniform conditions to a strong gradient, temporarily backtracking twice, and then a sudden jump back to uniform conditions. The two periods where the freeze-up stalls are associated with stronger northward flow through Bering Strait. The signature of the three inflow pathways is particularly evident at these times.

It is notable that, although evidence of polynyas exists in the mean concentration field, there is no clear mode that describes the occurrence of polynyas. Instead, the signature of the polynyas emerges in layers of increasing detail over many modes. An analysis over the full length of the AMSR2 record (2012–2020, not shown) reveals that the seasonal pattern is highly consistent. Spatial patterns of the mean and first two modes are nearly identical to those shown for the 2013–14 study year. Freeze-up always takes 2 months, while melt-back lasts 3–4 months. Melt-back is usually a smooth process, while freeze-up is often marked by interruptions.

5.2. Interconnectedness of local ice cover, wind forcing, and upwelling

The large-scale pattern of ice cover is dominated by the seasonal signal. To explore more localized features and their relationship to both wind and upwelling events, we also performed an EOF analysis of ice cover with a more limited spatial and temporal domain. Here, we consider ice concentration extending from 167.5°W to 151.5°W and 70°N to 73°N (corresponding to the box outlined in Fig. 8a), which contains all mooring sites except those in the southern Chukchi Sea and Bering Strait. Limiting the analysis to 15 Dec 2013 – 15 Jun 2014 (the season of nearly full ice cover for this spatial domain) eliminates the seasonal signal entirely and provides a look at the pattern of polynya formation.

5.2.1. Local ice EOF mode 1

Mode 1 (Fig. 9) for this more limited space/time domain accounts for 41% of the variance in the record. The structure shows regions of reduced ice cover adjacent to the coastline, consistent with the expected pattern of wind-driven coastal polynyas. The modal amplitude timeseries (Fig. 9b) shows a background condition in the positive state with intermittent excursions into the negative state, where the negative state corresponds to a reduction in ice concentration in the region of the polynyas. The background condition resides in the positive state due to a similar spatial pattern of slightly reduced ice concentration that shows up in the mean (not shown). Negative peaks match up well with the northeasterly wind events (Fig. 9b). We note that only four of the six events selected earlier for the upwelling analysis fall within the full-ice period, so we now consider all 12 events identified during this time (Table 3).

The mode 1 timeseries is positively correlated ($r = 0.46$) with the daily mean along-coast wind speed. Closer inspection, though, reveals that the correlation starts out much higher and diminishes over the season (Fig. 10a). From mid-Dec to mid-Feb, a period dominated by two strong wind events and large polynyas, the mode 1 timeseries is highly correlated with the wind ($r = 0.80$). From mid-Feb to mid-April, a period of weaker winds and much lower polynya response, the correlation is still good ($r = 0.55$). With the ice likely at its thickest and most tightly-packed state, a lower wind response is not surprising. From mid-April to mid-Jun, the correlation is low ($r = 0.25$, although still significant at the 95% confidence level). Strong along-coast winds are still associated with large a polynya response, but the polynyas do not close back up quickly when the wind dies down. At this time of year, the ice edge is approaching the southern part of the domain, indicating that conditions are becoming unfavorable for ice formation.

5.2.2. Mode 1 response relative to wind event strength

Recall that we characterized the strength of a wind event by the cumulative Ekman transport, which takes into account both the magnitude of the wind stress and the duration of the event. We now similarly quantify the polynya response as a cumulative modal excursion from the background state over the duration of the event:

$$CME = -\int_{t_s}^{t_e} M(t) - M_0 dt$$

where $M(t)$ is the value of the modal amplitude at time t and M_0 is the value of the modal amplitude in its background state. The sign is

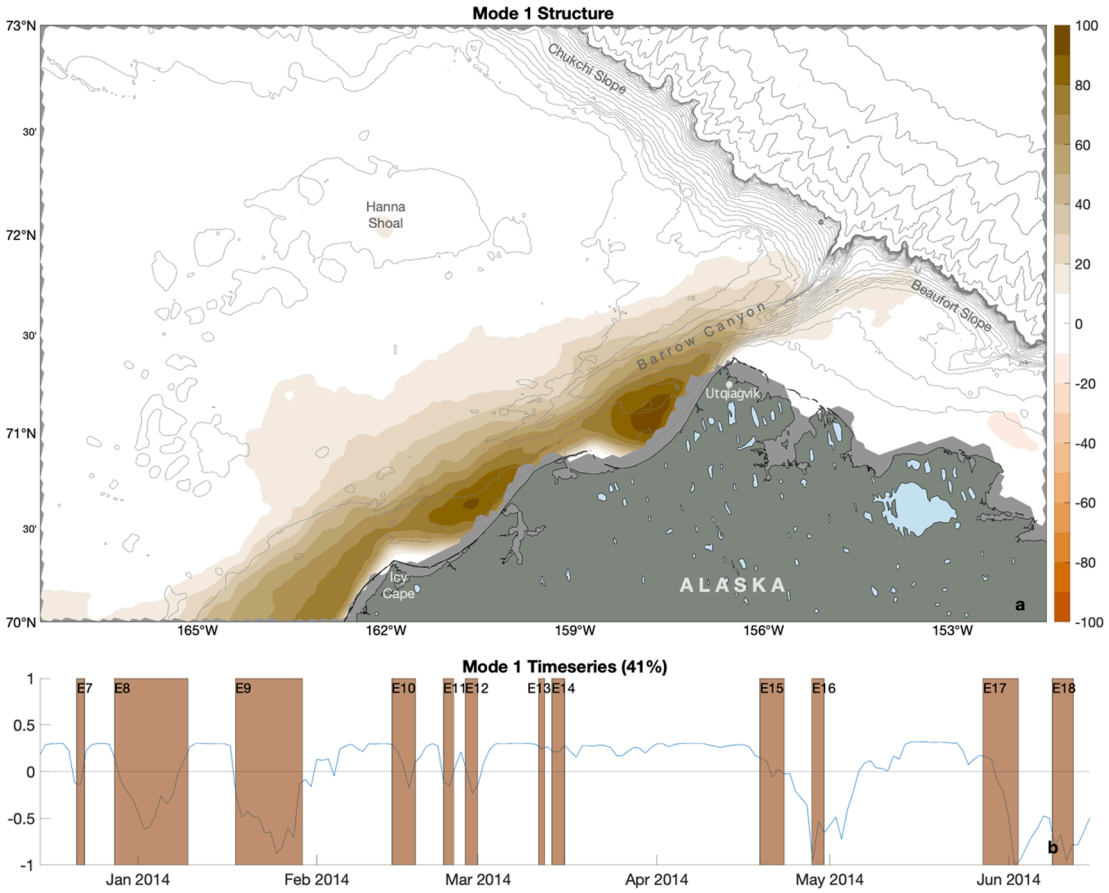

Fig. 9. Mode 1 of the local EOF of ice concentration over the full-ice period (15 Dec – 15 Jun). (a) Structure function. (b) Modal amplitude timeseries, where the shading indicates duration of northeasterly wind events identified at Utqiaġvik during this time period.

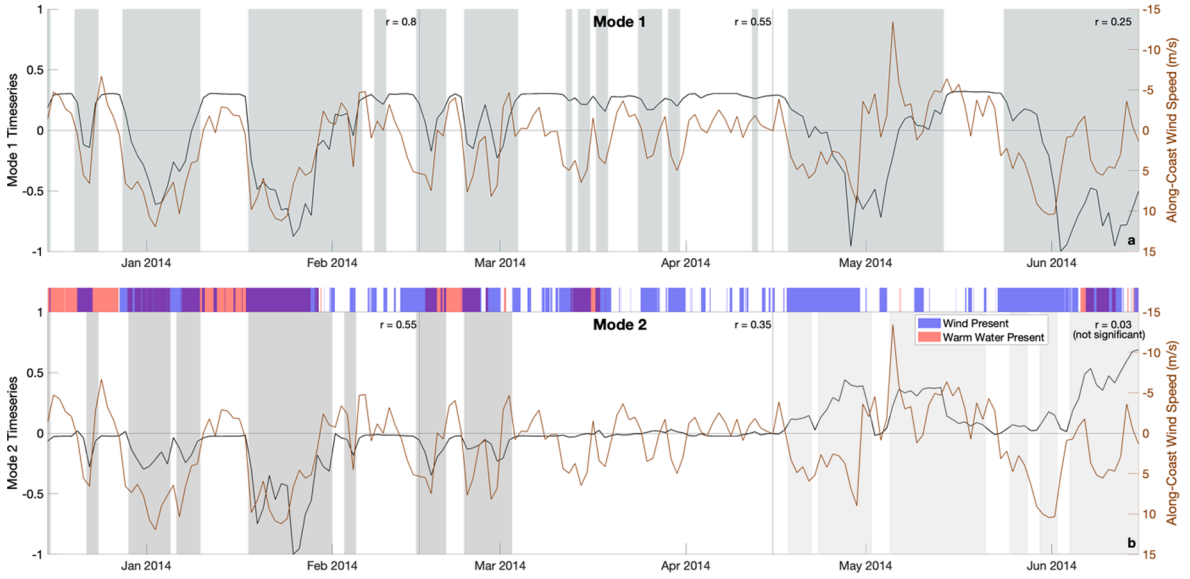

Fig. 10. Comparison of the local ice concentration EOF to potential forcing sources. (a) Mode 1 timeseries (black) and along-coast wind at Utqiaġvik (brown, inverted). Gray shading indicates negative excursions of the mode. (b) Mode 2 timeseries (black), along-coast wind at Utqiaġvik (brown, inverted). The dark gray shading indicates the negative excursions of the mode during the winter period. The light gray shading indicates the positive excursions of the mode during the spring period. The colors along the top depict when warm water was present at mooring C5 (red) and when positive along-coast wind occurred (blue). Overlapping of these two conditions results in purple segments. Correlation coefficients are noted for each two-month period in both (a) and (b), see text for details. (For interpretation of the references to color in this figure legend, the reader is referred to the web version of this article.)

reversed simply to produce a positive value for easier comparison with wind event strength. This reveals a clear linear relationship between the event strength (recall that we are considering all 12 wind events identified during this time) and the polynya response (Fig. 11). There are two major outliers to this relationship, E16 and E18. Both of these events occur towards the end of the full-ice season and are the second in a pair of events (Fig. 9b). As noted previously, at this time of year polynyas do not readily close when the wind speed decreases. At the start of each of these events, a polynya is still open from the previous event, enabling a much larger polynya to form than would otherwise be expected.

5.2.3. Local ice EOF mode 2

The orthogonal nature of EOF modes usually results in timeseries where a strong response in one mode corresponds to a time of little to no response in other modes. However, since polynyas tend towards being discrete events, the timing of the responses depicted in modes 1 and 2 of this EOF often coincide. However, the magnitude and/or sign of the response in each mode are quite different (as is the spatial pattern). Mode 2 (Fig. 12) accounts for 12% of the variance in the record. The structure shows a polynya response (a discrete area of decreased ice concentrations in the negative state) that extends from the head of Barrow Canyon westward across the shelf (centered near 71°N). The modal amplitude timeseries shows a background condition at a neutral state with excursions into the negative state in the winter and excursions into the positive state in the spring.

5.2.4. Winter polynyas

Since mode 2 shows some degree of response for nearly every polynya that mode 1 does, mode 2 also shows some correlation to along-coast wind speed (Fig. 10b). While the correlation between mode 2 and wind speed diminishes over the season just as it did with mode 1, the correlation for each time period is much lower. In fact, in the final two months, there is no significant correlation. Additionally, because the mode 2 polynya response is centered offshore and extends obliquely rather than parallel to the coast, it is not consistent with a wind-driven coastal polynya.

To explore the relationship between each of these modes and wind, we now take a closer look at wind direction when each mode shows an opening polynya (i.e., ice concentration is decreasing). As noted earlier, each mode exhibits a background state indicative of no polynya. We then identify periods of polynyas opening up as times when the modal amplitude for each mode exceeds a threshold below its background state and is lower than the previous day. If we look at the wind at all times when mode 1 is in its background state, we see that wind speeds are usually below 6 m s^{-1} and directions range from northwesterly to southwesterly (Fig. 13a), with few exceptions. By contrast, when mode 1 shows a polynya opening up, wind speeds are generally much higher, and the direction is almost exclusively northeasterly (Fig. 13b). Mode 2 shows a similar configuration of winds during opening of polynyas (Fig. 13d). This is not surprising, since both modes often show an opening polynya at the same time. However, during times when mode 2 is in its background state, winds can be from any direction, including northeasterly (Fig. 13c). This suggests that northeasterly winds are not the main factor inducing a polynya response in mode 2.

The location and shape of the mode 2 response is consistent with a melt-driven polynya associated with warm water being advected onto the shelf via Barrow Canyon. Temperature records along Barrow Canyon indicate some correspondence between the presence of warmer (above freezing) water and the mode 2 polynya response. The best relationship between water temperatures and mode 2 polynyas is seen at C5, which frequently receives RWW and AW during upwelling events and is also located near the leading edge of the mode 2 polynya. Yet, mode 2 only shows a polynya response about half of the time that warm water is present at C5. It is not until we put both the wind record and the temperature record at C5 together that a pattern emerges (colored bars in Fig. 10b). The mode 2 polynya response roughly corresponds to times when there is both a positive along-coast wind and warm water present at C5. The relationship is not perfect, but it must be kept in mind that the mooring temperature sensors are situated near the bottom and it is near-surface temperatures that would induce ice melt. Thus, we conclude that the mode 2 response represents the influence of warm water on wind-driven polynyas and that it is an indicator of upwelled warm water outcropping to the surface. More generally, reduced ice cover in such a pattern offshore could be used to identify warm water upwelling events in the absence of in situ measurements.

This assessment of both wind and warm water exerting influence on the recurring polynya near Barrow Canyon is consistent with the assertion by Hirano et al. (2016, 2018) that this is a hybrid latent and sensible heat polynya. The foundation of the argument that these authors make is that purely wind-driven (latent heat) polynyas are areas of constant ice production and so maintain frazil ice at their surface. These areas lose heat to the atmosphere as new ice is formed. The introduction of warm water, on the other hand, prevents ice production and creates areas of open water. In these areas, heat loss to the atmosphere is due to cooling of surface water. So, while areas of sensible and latent heat influence cannot be differentiated through atmospheric heat flux, areas of sensible heat influence can be identified by regions of open water. They then estimate the influence of warm water on the polynya by calculating sea ice production (based on atmospheric heat flux) with and without an open water mask. In both illustrated cases in the 2016 study and in the long term mean in the 2018 study, the region influenced by warm water masses based on identified areas of open water are quite localized and

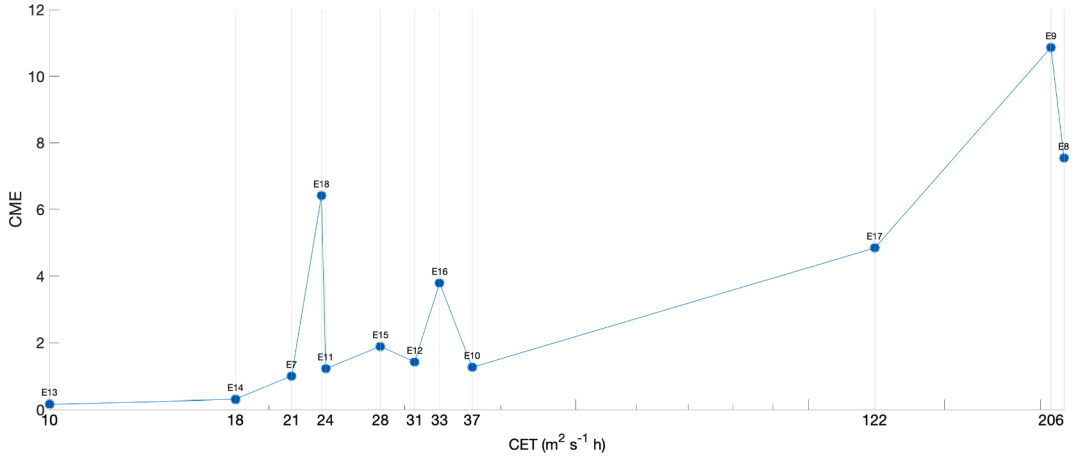

Fig. 11. Comparison of wind event strength (CET) to the local ice EOF mode 1 response (CME). CET is plotted on a log scale.

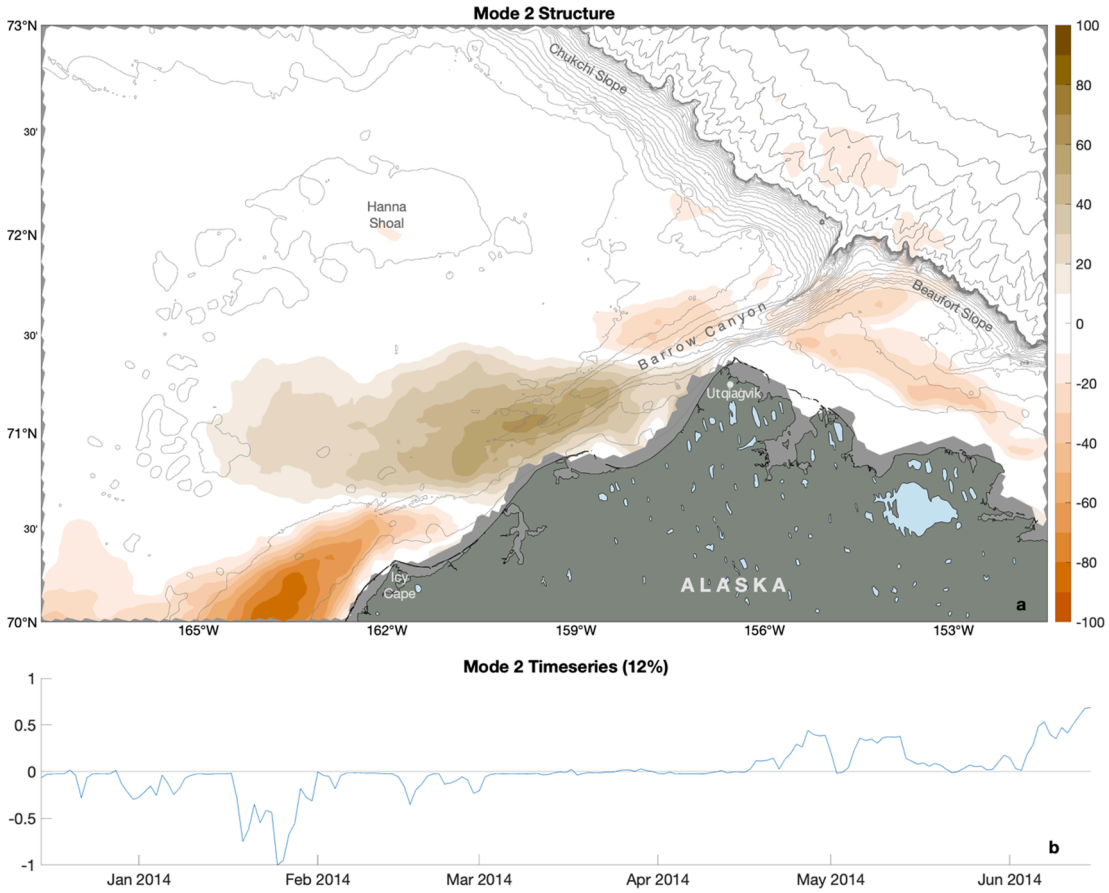

Fig. 12. Mode 2 of the local EOF of ice concentration over the full-ice period (15 Dec – 15 Jun). (a) Structure function. (b) Modal amplitude timeseries.

very near the coastline. The spatial structure of our mode 2 suggests a very different pattern of warm water influence. Ladd et al. (2016), based on four years of measurements at C1, also make an argument for a larger spatial extent of upwelled warm water influence on sea ice. Hirano et al. (2018) do show a single day in Jan. 2013 when the open water region extends farther offshore (to approximately 163°W at 71°N).

The assumption that the sensible heat influenced portion of the polynya can be identified by areas of open water seems to underestimate its spatial extent. The open water condition will not be met if the heat input from upwelled water masses is insufficient to completely melt the ice cover. This situation seems most likely in regions of ice convergence, such as would be expected on the margins of a wind-driven polynya. Areas where upwelled warm water results in incomplete melting of sea ice would not result in additional atmospheric heat flux, as all oceanic heat flux goes into melting ice, and so does not impact estimates of sea ice production. If ice is advected offshore and then melted in the area of upwelled water, this suggests a mechanism by which sustained ice production in a coastal polynya can result in no increase of ice across the shelf.

5.2.5. *Spring polynyas*

The reversal of sign in mode 2 in the spring indicates a regime change in polynya response that is not seen in mode 1. Similar to the negative winter excursions, the positive spring excursions of mode 2 occur intermittently within the mode 1 response (Fig. 10). Thus, they can also be viewed as an enhancement of the mode 1 polynyas. Whereas the winter polynyas tended to be focused around the head of Barrow Canyon, spring polynyas are focused at the southern end of the domain with a reduced polynya signature near Barrow Canyon. This is consistent with persistent NVWW in the canyon at this time (Fig. 7). The increased polynya activity at the southern end of the domain occurs as the ice edge is approaching and may be associated with an influx of warmer water through Bering Strait. Bottom temperatures at SCH (southern Chukchi Sea) begin to increase above freezing in mid-May, but we don't have enough information to draw a definitive conclusion there. While such a scenario would mark the transition of decreased ice concentrations from being polynya-related to melt-back related, the frequency of polynyas in this area mean that the two conditions often overlap. We note that, until the last week of the analysis, there is a distinct region of ice off of Cape Lisburne which separates the polynya formed/expanded during E17 from the ice edge and open water to the south.

5.2.6. *Limitations of this analysis*

The above analysis depicts a pattern of polynya formation that provides additional insight into the sensible heat vs. latent heat (wind-driven) influences to what previous studies have found. While we would prefer the two modes to cleanly describe the wind-driven and melt-driven portions of polynya formation without conflating the effects of an approaching ice edge, it is only through the combination of the southern enhancement due to the approaching ice edge and the warm-upwelling effect that a strong enough signal emerges. This is an important limitation of the results of this EOF analysis, and makes it sensitive to the choice of date range evaluated. A similar analysis for the full length of the AMSR2 record (2012–2020, not shown) exhibits similar spatial features. The first mode shows a polynya response parallel to the coastline nearly identical to that of the study year. However, the spatial pattern shown in mode 2 in the study year appears to be split between modes 2 and 3 in the longer record. In the longer record, mode 2 is a polynya response focused around the head of Barrow Canyon along with the southern enhancement that shows up in spring polynyas, and mode 3 is a polynya response centered offshore to the south of Barrow Canyon and extending westward. As such, the sum of modes 2 and 3 is

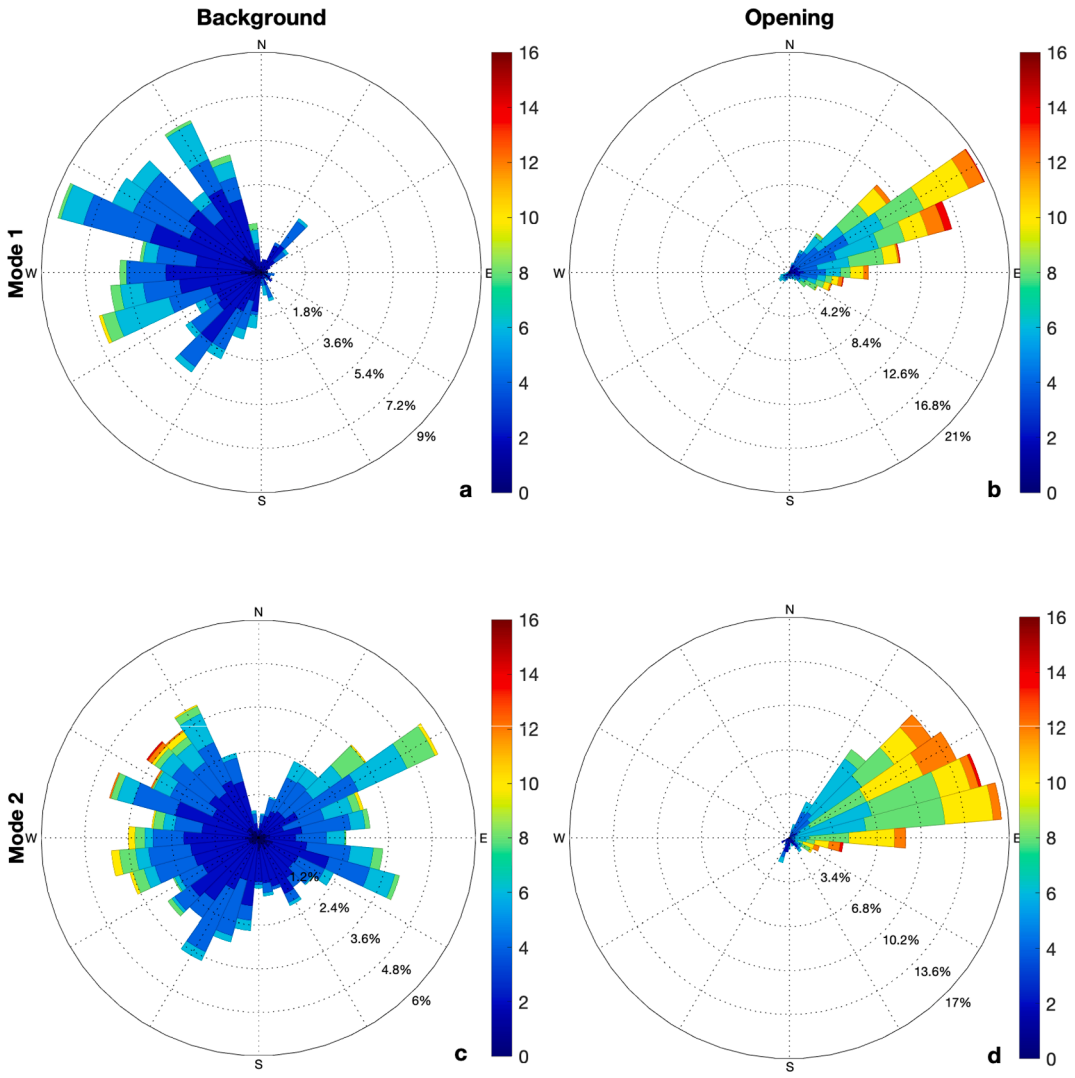

Fig. 13. Wind roses showing wind speed (color, m/s) and direction for wind at Utqiaġvik under various conditions of the local ice concentration EOF. The first row pertains to mode 1 and the second row pertains to mode 2. (a,c) Wind under background conditions, i.e., when the respective mode depicts no polynya response. (b,d) Wind while each mode depicts a polynya opening up.

similar to mode 2 for our study year. This likely reflects the fact that warm water is upwelled into Barrow Canyon more frequently than it is upwelled onto the shelf south of the canyon.

6. Shelf-wide response to wind forcing

Thus far it has been shown that northeasterly wind events are responsible for flow reversals in Barrow Canyon as well as the formation of polynyas along the coast. We now investigate variations in flow patterns across the full study area and explore their relationship to wind forcing. To do this, we performed an EOF analysis of hourly velocity (u and v) at all 25 moorings equipped with an ADCP (this excludes BCH in Barrow Canyon and SCH in the southern Chukchi Sea).

6.1. Velocity EOF mode 1

Mode 1, which explains 49% of the variability in the record, describes a coherent change in circulation across the entire domain. To compare the effect of the positive and negative states of this mode, we have added the structure function at ± 1 standard deviation of the modal amplitude to the mean velocities at each mooring (Fig. 14a-b). The positive 1 standard deviation state is largely an enhancement of the mean flow. Most moorings show a velocity around 2–3 times their mean, although the moorings just east of Hanna Shoal show little change. The negative 1 standard deviation state shows a reversal of flow in Barrow Canyon, at all of the sites south of Hanna Shoal and east of Central Channel (C1, C2, Bu, and C6), and at BS3 on the Beaufort Slope. There is still northward flow in Bering Strait, although it is reduced to about one third of the mean. Flow also slows across the northernmost parts of the shelf and the Chukchi Slope.

Although the positive state exceeds one standard deviation many times over the course of the year (Fig. 14c), it is usually only by a small amount. During the winter, the negative state frequently exceeds one standard deviation, many times by a large amount. At these stronger values of the negative state, flow reversal is seen at all of the mooring sites. This can result in strong southward flow in Bering Strait (up to 2.5 times stronger than the magnitude of the mean flow). East of Hanna Shoal and onto the upper Chukchi Slope, velocities remain small and the term “reversed” is somewhat subjective since flow here is far from rectilinear. Extreme flow reversals in Barrow Canyon and the nearby shelf can be close to ten times the magnitude of the mean flow.

6.2. Mode 1 relationship to regional wind

To explore the connection of the positive and negative state mode 1 flow regimes to wind forcing, we used the ERA5 10 m winds to create

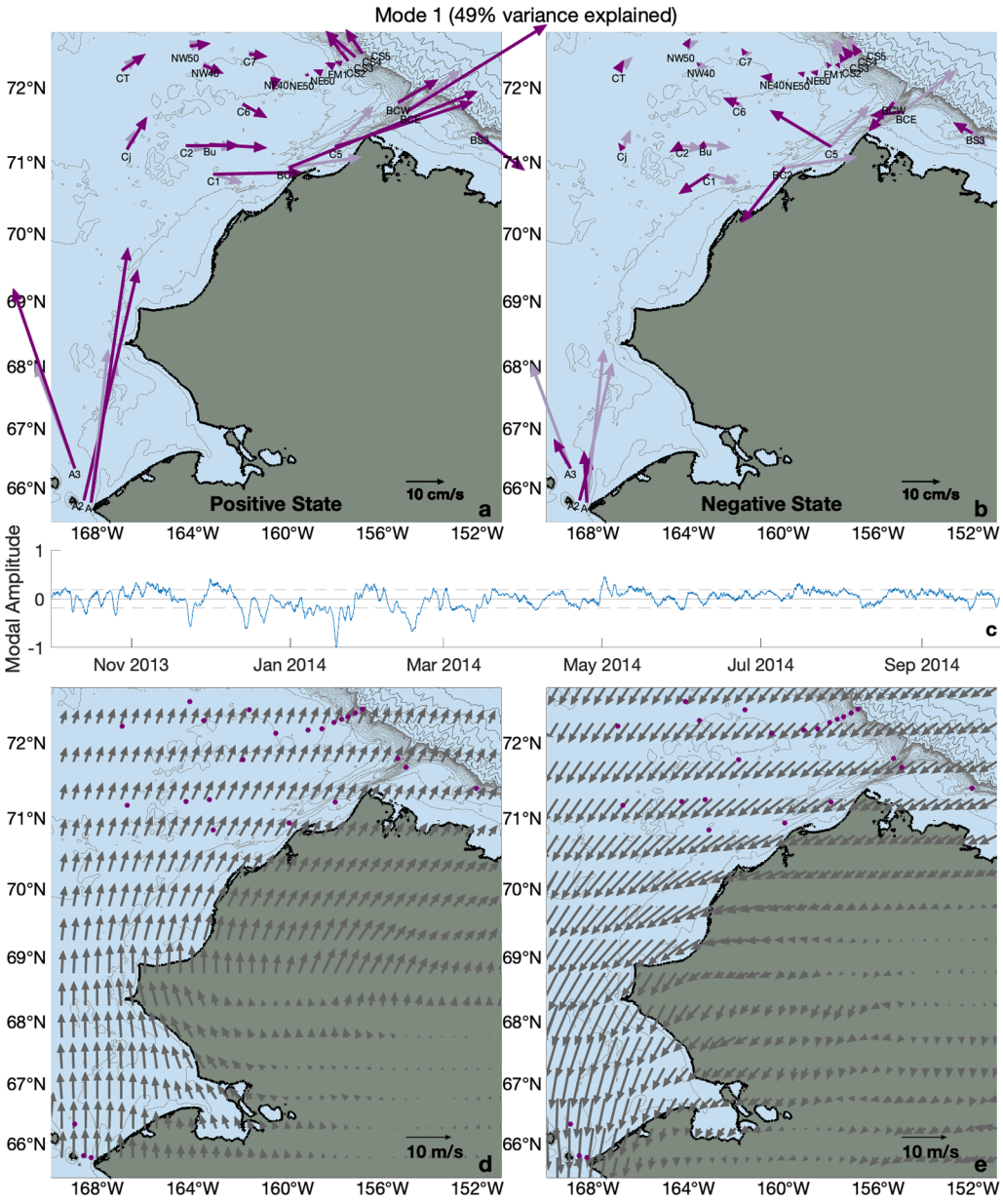

Fig. 14. EOF mode 1 of mooring velocities (a) Mean velocities shown in light purple, structure function at + 1 standard deviation added onto mean shown in dark purple. (b) Same as (a), but for −1 standard deviation. (c) Modal amplitude timeseries. (d) Composite ERA5 10 m wind field for all times when EOF mode 1 is above + 1 standard deviation. The mooring locations are indicated by purple dots. (e) Same as (d), but for all times below −1 standard deviation. (For interpretation of the references to color in this figure legend, the reader is referred to the web version of this article.)

composite wind maps for all times when the modal amplitude timeseries exceeded one standard deviation in each direction. When mode 1 is higher than one standard deviation above the mean (11.5% of record), the wind field composite (Fig. 14d) reveals a dominant southerly wind through Bering Strait, accounting for the enhanced northward flow there. The composite also shows the dominance of southwesterly wind along the northwest coastline of Alaska, enhancing the flow along the coastal pathway. Individual wind fields during these times (not shown) reveal that the wind actually varies from southwesterly to southeasterly. Mean winds along the northwest coastline of Alaska are northeasterly, so one would expect to see flow stronger than the mean under any other wind direction (consistent with the results of Lin et al., 2019a,b).

When mode 1 is lower than one standard deviation below the mean (14.8% of record), the wind field composite (Fig. 14e) reveals a dominant northerly wind through Bering Strait, accounting for reduced northward flow there (which is reversed in stronger negative states). The composite also shows the dominance of northeasterly wind along the northwest coast of Alaska, which accounts for the reversal of flow in Barrow Canyon (as shown in composites in Section 4.1). Therefore, mode 1 describes coherent circulation across the Chukchi Sea when winds that favor flow reversals in Barrow Canyon and Bering Strait are in phase with each other.

6.3. *Velocity EOF mode 2*

Mode 2, which explains 27% of the variability in the record, describes a less coherent change in circulation across the shelf. We have again added the structure function at ± 1 standard deviation of the modal amplitude to the mean velocities at each mooring (Fig. 15a-b). Similar to mode 1, the positive state is an enhancement of the mean flow across the northeastern Chukchi Sea. However, the northward flow in Bering Strait is reduced, reminiscent of the negative state in mode 1. Most moorings, including those east of Hanna Shoal, show velocity 1.5 to 2 times greater than their mean, whereas velocities in Bering Strait are approximately one third of their means. The negative state at 1 standard deviation shows enhanced northward flow in Bering Strait (about 1.5 times greater than the mean) and weak flow in Barrow Canyon, upstream at C1, and at BS3 on the Beaufort Slope. The rest of the moorings

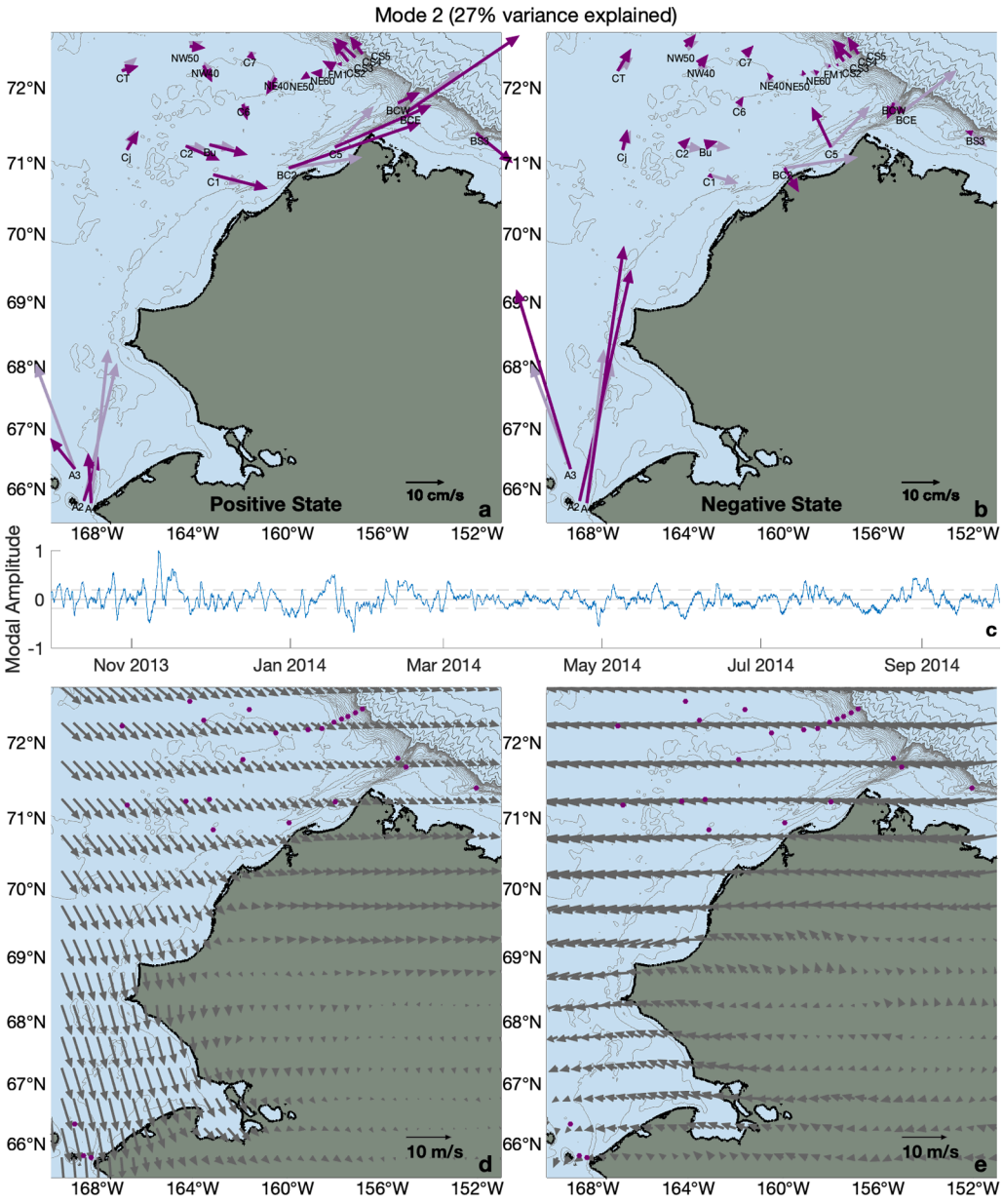

Fig. 15. EOF mode 2 of mooring velocities (a) Mean velocities shown in light purple, structure function at + 1 standard deviation added onto mean shown in dark purple. (b) Same as (a), but for −1 standard deviation. (c) Modal amplitude timeseries. (d) Composite ERA5 10 m wind field for all times when EOF mode 1 is above + 1 standard deviation. The mooring locations are indicated by purple dots. (e) Same as (d), but for all times below −1 standard deviation. (For interpretation of the references to color in this figure legend, the reader is referred to the web version of this article.)

south and east of Hanna Shoal show a slight decrease in velocities, while those north of Hanna Shoal show a slight increase.

Although the largest modal amplitude values for both the positive and negative states occur in the winter, both frequently exceed one standard deviation throughout the year (Fig. 15c). Stronger cases of the positive state show a reversal of flow in Bering Strait (up to 2.5 times the magnitude of the mean), and stronger cases of the negative state show a reversal of flow in Barrow Canyon and across the rest of the shelf (up to 2–3 times the magnitude of the mean).

6.4. Mode 2 relationship to regional wind

We now consider the composite wind fields for all times when the modal amplitude timeseries exceeded one standard deviation in each direction (Fig. 15d-e). When mode 2 is higher than one standard deviation above the mean (13.6% of record), recall that flow is enhanced relative to the mean circulation across most of the region, but reduced-to-reversed in Bering Strait. The wind field composite (Fig. 15d) reveals a dominant northerly wind in Bering Strait, accounting for the reduced-to-reversed flow there. The composite also shows the dominance of northwesterly winds along the northwest coastline of Alaska, which, as noted above, favors enhanced poleward flow in Barrow Canyon. Individual wind fields during these times (not shown) reveal that wind actually varies from southwesterly to northeasterly, converging on northwesterly as strength of the negative state increases.

When mode 2 is lower than one standard deviation below the mean (13.9% of record), recall that flow is reduced relative to the mean across most of the shelf and weak-to-reversed in Barrow Canyon, but enhanced in Bering Strait. The wind field composite (Fig. 15e) depicts very weak wind in Bering Strait. Individual wind fields (not shown) reveal that both northerly and southerly winds occur during these times. Northerly winds occur a higher proportion of the time, but tend to be weaker. Northerly winds become less common in more extreme cases of the negative state. Recall that the main driver of northward flow in Bering Strait is the Pacific-Arctic pressure head, and that the mean winds (northerly) oppose this flow. Weak northerly winds, therefore, result in northward flows above the annual mean. The wind composite reveals a dominant easterly wind along the northwest coast of Alaska. Individual

wind fields show that wind direction can be easterly to northeasterly, with northeasterly more common in stronger negative states. Therefore, mode 2 describes circulation during times when winds that favor flow reversals in Barrow Canyon and Bering Strait are out of phase with each other.

In the positive state of mode 2, the reduced northward flow in Bering Strait combined with enhanced down-canyon flow in Barrow Canyon would result in a divergence of flow somewhere in the south or central Chukchi Sea. The opposite flow regime in the negative state would result in a convergence of flow in the south or central Chukchi Sea. Weingartner et al. (1998) also note periods of apparent flow convergence seen in monthly averages of mooring velocities in Bering Strait, offshore of Cape Lisburne, and in upper Barrow Canyon. Without any velocity moorings in the south or central Chukchi Sea, we are unable to explore this further. However, Woodgate et al. (2005b) found a similar pair of EOF modes (using just the principal component of velocity at each mooring). That study, conducted in 1990–91, consisted of twelve moorings in three arrays: across Bering Strait, across the central Chukchi, and across the northern Chukchi (with significant gaps). It was unusual in that it included moorings in the western Chukchi (within the Russian EEZ), and offers us an interesting comparison. The dominant mode in their EOF described coherent flow in Bering Strait, the central Chukchi, and the northeastern Chukchi. Their second mode described times with opposing flow in different parts of the Chukchi. The eastern half of the central line was coherent with the head of Barrow Canyon, while the western half of the central line was coherent with Bering Strait and Long Strait (far western Chukchi). While the Woodgate et al. moorings were placed more than two decades prior to the moorings considered in this study, the similarity of the EOF analysis results suggest that the occurrence of these two spatial patterns is typical for the region.

6.5. *Differences between flow regimes in modes 1 and 2*

So far, we have discussed Mode 1 and 2 in terms of flow reversals. However, there are also differences in orientation of flow associated with each mode. To explore this, we will compare the direction in which circulation is altered from the mean at the extremes of each mode. The extremes are presented so as to maximize the contrast; one should bear in mind that the differences are generally more subtle. The direction of change for the maximum states of the two modes (Fig. 16a) allows us to see, under enhanced down-canyon flow in Barrow Canyon in both cases, the contrasting effects associated with northward and southward flow in Bering Strait. As noted previously for the positive states, flow across the northeast Chukchi is generally in the mean direction. However, southward flow in Bering Strait corresponds to a more southward shift in orientation of flow at most mooring locations across the shelf. At the minimum states of the two modes (Fig. 16b), flow in Barrow Canyon and across the shelf and slope is reversed. In this case, northward flow in Bering Strait corresponds to a reversal of flow across the shelf with a more northward shifted orientation. This shift in orientation does not affect moorings in Barrow Canyon, on the Beaufort Slope, or on the Chukchi Slope, where flow is more tightly bound to the bathymetry.

7. Summary

Through an expansive set of 27 moorings placed across the Chukchi Sea, adjacent slopes, and in the Bering Strait from 2013 to 2014, we have

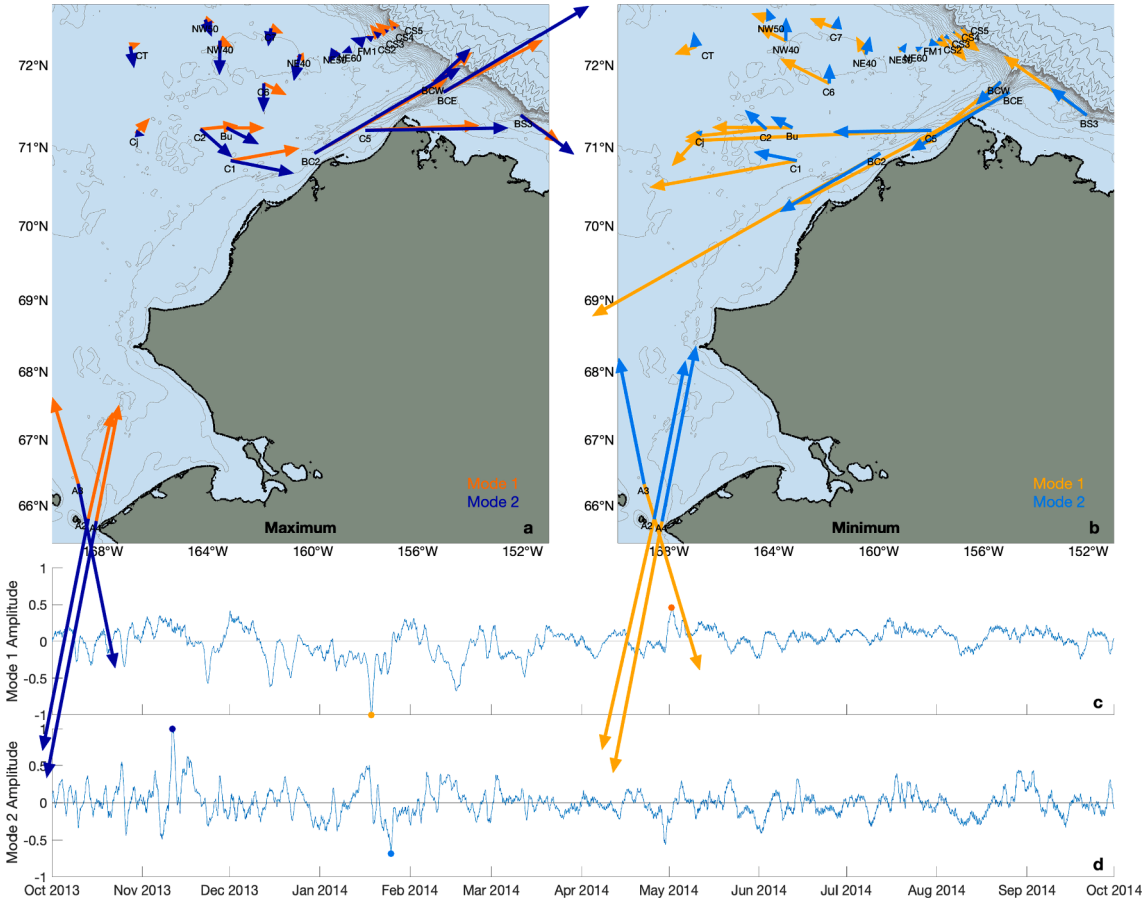

Fig. 16. Relative change in flow direction associated with EOF modes 1 and 2 of mooring velocities. (a) Change from mean velocity at maximum states. (b) Change from mean velocity at minimum states. (c,d) Modal amplitude timeseries for each mode. The points in time depicted by the mapped vectors are indicated by dots in the corresponding color.

been able to elucidate some of the controlling factors of the synoptic-scale circulation. While the primary driver of northward flow into the Chukchi Sea is the Pacific-Arctic pressure head, local winds have a strong influence over flow in the region. The most dramatic effect of local wind forcing is the upwelling in Barrow Canyon, which often draws both Pacific- and Atlantic-origin waters into the canyon. With several moorings along the length of the canyon, this study revealed the progression of upwelled water. Atlantic Water is frequently upwelled into Barrow Canyon in fall and winter, but is only occasionally delivered onto the shelf. In order for Atlantic Water to make it as far as the head of Barrow Canyon and onto the shelf, there must be a series of long upwelling events, with insufficient time between events for the upwelled water to fully drain from the canyon. Northeasterly wind is frequently implicated as the driver of these upwelling events. We find that while the velocity response in Barrow Canyon generally increases with increasing wind event strength, there are factors that complicate this relationship. These complications motivate further study of additional forcing mechanisms.

The same northeasterly winds that force upwelling in Barrow Canyon also drive polynya formation along the northwest coast of Alaska. However, polynyas in this region can also be influenced by the upwelling. Warm waters transported into Barrow Canyon can melt sea ice and enhance an existing polynya. This effect is especially dramatic when Atlantic Water is forced up onto the shelf. An EOF analysis of ice cover during the full-ice period enabled us to gauge the relative importance of wind-driven and sensible heat influences on polynyas in this area. The results suggest a much larger spatial extent of warm water influence than has been previously demonstrated. Our comparison with the local wind record also reveals a seasonally varying relationship between wind and the polynya response. While a larger spatial scale EOF analysis of ice cover mostly confirms the expected features of a seasonally ice-covered sea, it does provide a useful illustration that consolidates these features into a compact form. It also reveals that freeze-up occurs at a faster pace than melt-back and the inflow pathways have a similar spatial pattern of influence on ice cover during both time periods.

An EOF analysis of 25 mooring velocity records revealed two distinct modes of circulation. The first mode is associated with coherent flow across the region, with the positive state corresponding to enhancement of mean circulation, and the negative state showing a reversal of the mean circulation. The second mode describes times when flow in Barrow Canyon and Bering Strait oppose each other, i.e. one is slowed or reversed while the other is enhanced. Each state of the two modes is associated with a distinct regional wind pattern. Furthermore, whether flow anomalies in Bering Strait and Barrow Canyon are coherent or oppose each other has ramifications for flow across the rest of the shelf.

Quantifying the circulation of the Chukchi Sea and its relationship to wind and ice cover is critical for improving our understanding of the regional ecosystem. One aspect of our results that needs further explanation is the scatter in the relationship between wind event strength and the velocity response in Barrow Canyon. We have speculated that this may be related to northward propagating shelf waves originating in the Bering Sea, as suggested by Danielson et al. (2014). Wind direction along the northwest coastline of Alaska is typically uniform, but some of our data suggest that the times when it is not may be important in this regard. This is a topic of on-going study using our composite timeseries.

Declaration of Competing Interest

The authors declare that they have no known competing financial interests or personal relationships that could have appeared to influence the work reported in this paper.

Acknowledgements

A large number of technicians were responsible for the collection, processing, and quality control of the data that went into this study. The authors are extremely grateful to all of these individuals, and to the funding agencies that supported the respective field programs: The Bureau of Ocean Energy Management; The National Oceanic and Atmospheric Administration; The National Science Foundation; and The Japanese Agency for Marine-Earth Science and Technology. Support for this analysis was provided by the following grants: National Oceanic and Atmospheric Administration grant NA14OAR4320158; National Science Foundation grant OPP-1733564.

References

Aagaard, K., Roach, A.T., 1990. Arctic ocean-shelf exchange: Measurements in Barrow Canyon. J. Geophys. Res. 95 (C10), 18163. https://doi.org/10.1029/JC095iC10p18163.

Beitsch, A., Kaleschke, L., Kern, S., 2014. Investigating High-Resolution AMSR2 Sea Ice Concentrations during the February 2013 Fracture Event in the Beaufort Sea. Remote Sensing 6 (5), 3841–3856. https://doi.org/10.3390/rs6053841.

Bourke, R.H., Paquette, R.G., 1976. Atlantic water on the Chukchi Shelf. Geophys. Res. Lett. 3 (10), 629–632. https://doi.org/10.1029/GL003i010p00629.

Coachman, L.K., Aagaard, K., 1966. On the water exchange through Bering Strait. Limnol. Oceanogr. 11 (1), 44–59. https://doi.org/10.4319/lo.1966.11.1.0044.

Danielson, S.L., Weingartner, T.J., Hedstrom, K.S., Aagaard, K., Woodgate, R., Curchitser, E., Stabeno, P.J., 2014. Coupled wind-forced controls of the Bering-Chukchi shelf circulation and the Bering Strait throughflow: Ekman transport, continental shelf waves, and variations of the Pacific-Arctic sea surface height gradient. Prog. Oceanogr. 125, 40–61. https://doi.org/10.1016/j.pocean.2014.04.006.

Fang, Y., Weingartner, T.J., Dobbins, E.L., Winsor, P., Statscewich, H., Potter, R.A., Mudge, T.D., Stoudt, C.A., Borg, K., 2020. Circulation and Thermohaline Variability of the Hanna Shoal Region on the Northeastern Chukchi Sea Shelf. J. Geophys. Res. Oceans 125 (7). https://doi.org/10.1029/2019JC015639.

Frey, K.E., Moore, G.W.K., Cooper, L.W., Grebmeier, J.M., 2015. Divergent patterns of recent sea ice cover across the Bering, Chukchi, and Beaufort seas of the Pacific Arctic Region. Prog. Oceanogr. 136, 32–49. https://doi.org/10.1016/j.pocean.2015.05.009.

Gong, D., Pickart, R.S., 2016. Early summer water mass transformation in the eastern Chukchi Sea. Deep Sea Res. Part II 130, 43–55. https://doi.org/10.1016/j.dsr2.2016.04.015.

Grebmeier, J.M., Cooper, L.W., Feder, H.M., Sirenko, B.I., 2006. Ecosystem dynamics of the Pacific-influenced Northern Bering and Chukchi Seas in the Amerasian Arctic. Prog. Oceanogr. 71 (2–4), 331–361. https://doi.org/10.1016/j.pocean.2006.10.001.

Hersbach, H., Bell, B., Berrisford, P., Hirahara, S., Horányi, A., Muñoz-Sabater, J., Nicolas, J., Peubey, C., Radu, R., Schepers, D., Simmons, A., Soci, C., Abdalla, S., Abellan, X., Balsamo, G., Bechtold, P., Biavati, G., Bidlot, J., Bonavita, M., Chiara, G., Dahlgran, P., Dee, D., Diamantakis, M., Dragani, R., Flemming, J., Forbes, R., Fuentes, M., Geer, A., Haimberger, L., Healy, S., Hogan, R., Hólm, E., Janisková, M., Keeley, S., Laloyaux, P., Lopez, P., Lupu, C., Radnoti, G, Rosnay, P., Rozum, I., Vamborg, F., Villaume, S., Thépaut, J., 2020. The ERA5 global reanalysis. Q. J. R. Meteorolog. Soc. 146 (730), 1999–2049. https://doi.org/10.1002/qj.3803.

Hirano, D., Fukamachi, Y., Ohshima, K.I., Watanabe, E., Mahoney, A.R., Eicken, H., Itoh, M., Simizu, D., Iwamoto, K., Jones, J., Takatsuka, T., Kikuchi, T., Tamura, T., 2018. Winter Water Formation in Coastal Polynyas of the Eastern Chukchi Shelf: Pacific and Atlantic Influences. J. Geophys. Res. Oceans 123 (8), 5688–5705. https://doi.org/10.1029/2017JC013307.

Hirano, D., Fukamachi, Y., Watanabe, E., Ohshima, K.I., Iwamoto, K., Mahoney, A.R., Eicken, H., Simizu, D., Tamura, T., 2016. A wind-driven, hybrid latent and sensible heat coastal polynya off Barrow, Alaska. J. Geophys. Res.: Oceans 121 (1), 980–997. https://doi.org/10.1002/2015JC011318.

Itoh, M., Nishino, S., Kawaguchi, Y., Kikuchi, T., 2013. Barrow Canyon volume, heat, and freshwater fluxes revealed by long-term mooring observations between 2000 and 2008: BARROW CANYON FLUXES FOR 2000–2008. J. Geophys. Res. Oceans 118 (9), 4363–4379. https://doi.org/10.1002/jgrc.20290.

Itoh, M., Shimada, K., Kamoshida, T., McLaughlin, F., Carmack, E., Nishino, S., 2012. Interannual variability of Pacific Winter Water inflow through Barrow Canyon from 2000 to 2006. J. Oceanogr. 68 (4), 575–592. https://doi.org/10.1007/s10872-012-0120-1.

Ladd, C., Mordy, C.W., Salo, S.A., Stabeno, P.J., 2016. Winter Water Properties and the Chukchi Polynya: WATER PROPERTIES AND CHUKCHI POLYNYA. J. Geophys. Res. Oceans 121 (8), 5516–5534. https://doi.org/10.1002/2016JC011918.

Li, M., Pickart, R.S., Spall, M.A., Weingartner, T.J., Lin, P., Moore, G.W.K., Qi, Y., 2019. Circulation of the Chukchi Sea shelfbreak and slope from moored timeseries. Prog. Oceanogr. 172, 14–33. https://doi.org/10.1016/j.pocean.2019.01.002.

Lin, P., Pickart, R.S., McRaven, L.T., Arrigo, K.R., Bahr, F., Lowry, K.E., Stockwell, D.A., Mordy, C.W., 2019a. Water Mass Evolution and Circulation of the Northeastern Chukchi Sea in Summer: Implications for Nutrient Distributions. J. Geophys. Res. Oceans 124 (7), 4416–4432. https://doi.org/10.1029/2019JC015185.

Lin, P., Pickart, R.S., Moore, G.W.K., Spall, M.A., Hu, J., 2019b. Characteristics and dynamics of wind-driven upwelling in the Alaskan Beaufort Sea based on six years of mooring data. Deep Sea Res. Part II 162, 79–92. https://doi.org/10.1016/j.dsr2.2018.01.002.

Lin, P., Pickart, R.S., Stafford, K.M., Moore, G.W.K., Torres, D.J., Bahr, F., Hu, J., 2016. Seasonal variation of the Beaufort shelfbreak jet and its relationship to Arctic cetacean occurrence: SEASONAL VARIATION OF THE BEAUFORT JET. J. Geophys.

Res. Oceans 121 (12), 8434–8454. https://doi.org/10.1002/jgrc.v121.1210.1002/2016JC011890.
Moore, S.E., Stabeno, P.J., 2015. Synthesis of Arctic Research (SOAR) in marine ecosystems of the Pacific Arctic. Prog. Oceanogr. 136, 1–11. https://doi.org/10.1016/j.pocean.2015.05.017.
Morales Maqueda, M.A., Willmott, A.J., Biggs, N.R.T., 2004. Polynya Dynamics: A Review of Observations and Modeling. Rev. Geophys. 42 (1) https://doi.org/10.1029/2002RG000116.
Nikolopoulos, A., Pickart, R.S., Fratantoni, P.S., Shimada, K., Torres, D.J., Jones, E.P., 2009. The western Arctic boundary current at 152°W: Structure, variability, and transport. Deep Sea Res. Part II 56 (17), 1164–1181. https://doi.org/10.1016/j.dsr2.2008.10.014.
Pacini, A., Moore, G.W.K., Pickart, R.S., Nobre, C., Bahr, F., Våge, K., Arrigo, K.R., 2019. Characteristics and Transformation of Pacific Winter Water on the Chukchi Sea Shelf in Late Spring. J. Geophys. Res. Oceans 124 (10), 7153–7177. https://doi.org/10.1029/2019JC015261.
Pawlowicz, R., Beardsley, B., Lentz, S., 2002. Classical tidal harmonic analysis including error estimates in MATLAB using T_TIDE. Comput. Geosci. 28 (8), 929–937. https://doi.org/10.1016/S0098-3004(02)00013-4.
Pickart, R.S., Moore, G.W.K., Mao, C., Bahr, F., Nobre, C., Weingartner, T.J., 2016. Circulation of winter water on the Chukchi shelf in early Summer. Deep Sea Res. Part II 130, 56–75. https://doi.org/10.1016/j.dsr2.2016.05.001.
Pickart, R.S., Nobre, C., Lin, P., Arrigo, K.R., Ashjian, C.J., Berchok, C., Cooper, L.W., Grebmeier, J.M., Hartwell, I., He, J., Itoh, M., Kikuchi, T., Nishino, S., Vagle, S., 2019. Seasonal to mesoscale variability of water masses and atmospheric conditions in Barrow Canyon, Chukchi Sea. Deep Sea Res. Part II 162, 32–49. https://doi.org/10.1016/j.dsr2.2019.02.003.
Pickart, R.S., Schulze, L.M., Moore, G.W.K., Charette, M.A., Arrigo, K.R., van Dijken, G., Danielson, S.L., 2013. Long-term trends of upwelling and impacts on primary productivity in the Alaskan Beaufort Sea. Deep Sea Res. Part I 79, 106–121. https://doi.org/10.1016/j.dsr.2013.05.003.
Pisareva, M.N., Pickart, R.S., Lin, P., Fratantoni, P.S., Weingartner, T.J., 2019. On the nature of wind-forced upwelling in Barrow Canyon. Deep Sea Res. Part II 162, 63–78. https://doi.org/10.1016/j.dsr2.2019.02.002.
Serreze, M.C., Crawford, A.D., Stroeve, J.C., Barrett, A.P., Woodgate, R.A., 2016. Variability, trends, and predictability of seasonal sea ice retreat and advance in the Chukchi Sea: SEA ICE IN THE CHUKCHI SEA. J. Geophys. Res. Oceans 121 (10), 7308–7325. https://doi.org/10.1002/2016JC011977.
Spall, M.A., 2007. Circulation and water mass transformation in a model of the Chukchi Sea. J. Geophys. Res. 112 (C5), C05025. https://doi.org/10.1029/2005JC003364.
Spreen, G., Kaleschke, L., Heygster, G., 2008. Sea ice remote sensing using AMSR-E 89-GHz channels. J. Geophys. Res. 113 (C2), C02S03. https://doi.org/10.1029/2005JC003384.
Tian, F., Pickart, R.S., Lin, P., Pacini, A., Moore, G.W.K., Stabeno, P., Weingartner, T., Itoh, M., Kikuchi, T., Dobbins, E., Bell, S., Woodgate, R.A., Danielson, S.L., Wang, Z., 2021. Mean and Seasonal Circulation of the Eastern Chukchi Sea From Moored Timeseries in 2013–2014. J. Geophys. Res. Oceans 126 (5). https://doi.org/10.1029/2020JC016863.
Weingartner, T.J., Cavalieri, D.J., Aagaard, K., Sasaki, Y., 1998. Circulation, dense water formation, and outflow on the northeast Chukchi Shelf. J. Geophys. Res. Oceans 103 (C4), 7647–7661. https://doi.org/10.1029/98JC00374.
Weingartner, T.J., Potter, R.A., Stoudt, C.A., Dobbins, E.L., Statscewich, H., Winsor, P.R., Mudge, T.D., Borg, K., 2017. Transport and thermohaline variability in Barrow Canyon on the Northeastern Chukchi Sea Shelf: BARROW CANYON CURRENTS AND WATER MASSES. J. Geophys. Res. Oceans 122 (5), 3565–3585. https://doi.org/10.1002/2016JC012636.
Woodgate, R., 2012. Arctic Ocean Circulation – going around at the top of the world. 15.
Woodgate, R.A., 2018. Increases in the Pacific inflow to the Arctic from 1990 to 2015, and insights into seasonal trends and driving mechanisms from year-round Bering Strait mooring data. Prog. Oceanogr. 160, 124–154. https://doi.org/10.1016/j.pocean.2017.12.007.
Woodgate, R.A., Aagaard, K., Weingartner, T.J., 2005a. Monthly temperature, salinity, and transport variability of the Bering Strait through flow: BERING STRAIT THROUGH FLOW. Geophys. Res. Lett. 32 (4), n/a–n/a. https://doi.org/10.1029/2004GL021880.
Woodgate, R.A., Aagaard, K., Weingartner, T.J., 2005b. A year in the physical oceanography of the Chukchi Sea: Moored measurements from autumn 1990–1991. Deep Sea Res. Part II 52 (24–26), 3116–3149. https://doi.org/10.1016/j.dsr2.2005.10.016.
Woodgate, R.A., Weingartner, T., Lindsay, R., 2010. The 2007 Bering Strait oceanic heat flux and anomalous Arctic sea-ice retreat: 2007 BERING STRAIT OCEANIC HEAT FLUX. Geophys. Res. Lett. 37 (1), n/a–n/a. https://doi.org/10.1029/2009GL041621.
Woodgate, R., Stafford, K., Prahl, F., 2015. A Synthesis of Year-Round Interdisciplinary Mooring Measurements in the Bering Strait (1990–2014) and the RUSALCA Years (2004–2011). Oceanography 28 (3), 46–67. https://doi.org/10.5670/oceanog10.5670/oceanog.201510.5670/oceanog.2015.57.